

The Origin of Diffuse X-ray and γ -ray Emission from the Galactic Center Region: Cosmic Ray Particles

F. Yusef-Zadeh¹, M. Muno², M. Wardle³, D.C. Lis⁴

ABSTRACT

The inner couple hundred pcs of our Galaxy is characterized by significant amount of synchrotron-emitting gas, which appears to co-exist with a large reservoir of molecular gas. Many of the best studied sources in this region exhibit a mixture of 6.4 keV Fe $K\alpha$ emission, molecular line emission and nonthermal radio continuum radiation. The spatial correlation between fluorescent Fe $K\alpha$ line emission at 6.4 keV and molecular line emission from Galactic center molecular clouds has been explained as reflected X-rays from a past outburst of Sgr A*. Here we present multi-wavelength study of a representative Galactic center cloud Sgr C using *Chandra*, *VLA* and *FCRAO*. We note a correlation between the nonthermal radio filaments in Sgr C and the X-ray features, suggesting that the two are related. This correlation, when combined with the distribution of molecular gas suggests against the irradiation of Sgr C by Sgr A*. Instead, we account for this distribution in terms of the impact of the relativistic particles from local (nonthermal filaments) and extended sources with diffuse neutral gas producing both a nonthermal bremsstrahlung X-ray continuum emission, as well as diffuse 6.4 keV line emission. The production rate of Fe $K\alpha$ photons associated with the injection of electrons into a cloud as a function of column density is calculated. The required energy density of low-energy cosmic rays associated with the synchrotron emitting radio filaments or extended features is estimated to be in the range between 20 and $\sim 10^3$ eV cm⁻³ for Sgr C, Sgr B1, Sgr B2,

¹Department of Physics and Astronomy, Northwestern University, Evanston, IL 60208 (zadeh@northwestern.edu)

²Dept Physics and Astronomy, University of California, Los Angeles, Box 951547, Los Angeles, CA 90095 (mmuno@astro.ucla.edu)

³Department of Physics, Macquarie University, Sydney NSW 2109, Australia (wardle@physics.mq.edu.au)

⁴California Institute of Technology, MC 320-47, Pasadena, CA 91125 (dcl@caltech.edu)

and “the 45 and -30 km s⁻¹” clouds. We also generalize this idea to explain the cosmic-ray heating of molecular gas, the interstellar cosmic ray ionization, the pervasive production of diffuse K α line and TeV emission from the Galactic center molecular clouds. In particular, we suggest that Inverse Compton scattering of the sub-millimeter radiation from dust by relativistic electrons may contribute substantially to the large-scale diffuse TeV emission observed towards the central regions of the Galaxy.

Subject headings: Galaxy: center - H II regions - ISM: general - ISM - X-rays - cosmic rays

1. Introduction

It is well recognized that the Galactic center region hosts several sources of energetic activity in the form of nonthermal linear filaments, supernova remnants and colliding winds of massive stars. This region is also recognized to be the site of massive molecular clouds with pockets of on-going and past massive star formation. The most prominent of these clouds are associated with Sgr B2, Sgr C, as well as the clouds associated with radio continuum arc and Sgr A. Sgr C or G359.43–0.09 is one of the best examples of a massive star-forming region which hosts prominent thermal and nonthermal radio continuum, millimeter, sub-millimeter and X-ray sources in the Galactic center region. This massive star forming region is identified by its H II region, a dense molecular cloud and nonthermal radio filaments. This source is also known as an X-ray source based on ASCA observations (Murakami et al. 2001a) showing the evidence of iron K-shell fluorescence (K α) line emission. To probe the nature of high-energy activity in the Galactic center region, we have selected to study Sgr C in detail, as well as star forming regions near the continuum arc ($l \sim 0.2^\circ$) and the Sgr B complex.

Sgr C consists of a thermal radio continuum, a far-IR and a sub-millimeter source, as well as a synchrotron emitting source associated with magnetized filaments (Odenwald & Fazio 1984; Caswell & Haynes 1987; Liszt 1992; Tsuboi et al. 1991; Lis & Carlstrom 1994). The Sgr C H II complex is thought to be powered by a single O4 ZAMS star. The molecular mass of Sgr C is estimated to be $\sim 5 - 6 \times 10^5 M_\odot$ with column density of $N_{\text{H}_2} \sim 10^{23} \text{ cm}^{-2}$, based on sub-millimeter and ¹³CO observations (Liszt & Spiker 1995; Lis & Carlstrom 1994). Recent radio continuum survey of the Galactic center region has identified additional nonthermal filaments distributed in the immediate vicinity of the Sgr C H II region (Nord et al. 2004; Yusef-Zadeh, Hewitt & Cotton 2004). The main nonthermal radio filament (NRF) appears to end abruptly inside the Sgr C molecular H II complex M359.5–0.15 with a velocity

of -65 km s^{-1} (Liszt & Spiker 1995). Similar radio recombination line velocity has also been detected from the Sgr C H II region (Anantharamaiah & Yusef-Zadeh 1989). HI absorption measurements toward the nonthermal filament and the H II region constrain the distance to both sources within the inner 200 pc of the Galactic center. However, Roy (2003) suggests that the Sgr C filament and H II region are two separate objects and may not be interacting with each other (Roy 2003).

The ASCA measurements show the presence of strong fluorescent 6.4 keV line emission from neutral iron gas implying H_2 column density similar to that of molecular line observations (Murakami et al. 2001a). The nature of the 6.4 keV line emission has been considered to be due to the irradiation of the Sgr C molecular cloud originated by past energetic outburst from Sgr A* (Murakami et al. 2001a). Similar mechanism has been postulated to explain the origin of the strong 6.4 keV line emission detected from other Galactic center molecular clouds (e.g., Sgr B2) by either Sgr A* or from the interaction of the Sgr A East and “the 50 km s^{-1} cloud” (Koyama et al. 1996; Murakami et al. 2000, 2001b; Revnivtsev et al. 2004; Fryer et al. 2006). An alternative explanation to the X-ray reflection nebula model has accounted for the origin of X-ray emission in terms of the impact of low-energy cosmic ray particles with neutral gas associated with the M0.11–0.08 molecular cloud (Yusef-Zadeh, Law & Wardle 2002). These authors speculated that the same process could also explain the origin of the 6.4 keV line emission from other Galactic center molecular clouds.

The structure of this paper is as follows. In §2, we re-analyze the archival *Chandra* observations of the Galactic center region followed by the analysis of new millimeter line and radio continuum data using FCRAO and VLA. In §3, we report the discovery of X-ray filamentary structures in Sgr C. The morphology of X-ray and nonthermal radio continuum features suggest that many of the $\text{K}\alpha$ 6.4 keV line features lie near the nonthermal radio filaments at 20 and 90 cm wavelengths. We also examine the morphology of ^{13}CO and Fe $\text{K}\alpha$ lines and estimate column densities using millimeter and X-ray techniques. We present spectral index determination in §3.1.5 and polarization measurements of the brightest filament in Sgr C at radio wavelengths in the Appendix. The synchrotron parameters of the Sgr C filament is critical in support of our picture that the low-energy component of the synchrotron emitting particles penetrate molecular clouds. We then compare the distribution of 6.4 keV and TeV emission from prominent galactic center molecular clouds. The overall correlations of $\text{K}\alpha$ line emission, molecular line emission from the “45 and -30 km s^{-1} clouds”, TeV emission and nonthermal radio continuum features are described. In §4, we argue in support of enhanced cosmic rays in the central region of the Galaxy and compare the irradiation model versus the low-energy cosmic ray model to account for the origin of the 6.4 keV emission. We then describe a quantitative mode of injection of cosmic rays into molecular clouds and the subsequent heating of gas before this model is applied to the

Galactic center molecular clouds. Unlike the irradiation model, the picture that is presented here can naturally explain the high temperature of molecular gas in the galactic center region. Lastly, we investigate the origin of diffuse TeV emission from Galactic center clouds in terms of the inverse Compton scattering of dust emission by the high energy component of the cosmic rays distributed throughout this unique region of the Galaxy.

2. Data Reductions

2.1. X-ray Analysis

Sgr C was observed with the *Chandra* Advanced CCD Imaging Spectrometer (ACIS-I) (Weisskopf et al. 2002) as part of the shallow Galactic center survey (Wang et al. 2002) with two overlapping 11 ks exposures on 2001 July 20 (sequences 2270 and 2272). We reduced the observation using standard tools that are part of CIAO version 3.2. We first created a cleaned event list from the ACIS-I array for each observation. We corrected the pulse heights of the events for position-dependent charge-transfer inefficiency (Townsend et al. 2002) and excluded events that did not pass the standard ASCA grade filters and *Chandra* X-ray center (CXC) good-time filters. We searched for intervals during which the background rate flared to $\geq 3\sigma$ above the mean level, and found none. Our goal was to study the properties of diffuse features, so we removed events within circles enclosing at least 92% of the point-spread function that were centered at the locations of the point-like X-ray sources, as identified by Munro et al. (2006). Finally, we re-projected the events from each observation onto a fixed tangent point (the location of Sgr A*), so that they could be combined to form composite images.

We then generated images of the continuum emission between 4–8 keV, excluding the 6.10–7.15 keV energy range containing iron lines, with a resolution of $9''$. In addition to the continuum images, we also made the Fe K- α flux and equivalent width images. Both the continuum and line flux images were made the same way. For display purposes, the holes left in the image when we excluded point sources were filled with pixel values drawn from a Poisson distribution that had the mean value of the pixels in a surrounding annulus. We repeated the same process on an image of an exposure image generated with standard CIAO tools, and then divided the count image by the resulting exposure image in order to create a flux image of the diffuse emission. Finally, we present two different types of images, one of which is adaptively smoothed using the CIAO tool *csmooth*, whereas the other is convolved with $30''$ Gaussians.

Images of the equivalent widths of the low-ionization 6.4 keV line of Fe were constructed

using the techniques described by Park et al. (2004). Adaptively-smoothed images of the diffuse line emission were generated in the same manner as the continuum image, using the 6.25–6.50 keV band for Fe K- α . The continuum under each line was computed based on adaptively-smoothed images of the flux in the 5.0–6.1 keV and 7.15–7.30 keV energy bands. We assumed that the flux in each continuum band (F_{band}) could be described as a power law, so that the normalization (N) and slope (Γ) of the power law could be computed from

$$F_{\text{band}} = \frac{NE_{\text{low}}^{-\Gamma+1} - NE_{\text{high}}^{-\Gamma+1}}{\Gamma - 1}. \quad (1)$$

Using the fluxes in both continuum bands, the above equation was solved for N and Γ using Newton’s algorithm, and the parameters were used to estimate the continuum contribution to the line emission images. To derive the equivalent width images, we subtracted the estimated total continuum flux from the line image, and then divided the line image by the continuum flux density at the centroid of the line (6.4 keV). We caution that we have neglected the cosmic-ray background in generating these maps, which could account as much as $\sim 40\%$ of the events in the 6–7 keV band, and consequently biases any estimate of the equivalent width. The assumption of a power law spectrum also introduces a small systematic bias in these maps. We have not attempted to correct these effects, because they are only used to search for regions of enhanced iron emission.

In order to confirm the properties suggested by the images of the diffuse line and continuum emission, we examined the spectra of small regions of the image. For each observation, counts were extracted from each region of interest, and then binned as a function of pulse-height to create spectra. We obtained the response functions from Townsley et al. (2002) and averaged them weighted by the number of counts received by the relevant portions of the detectors. Effective area functions for the spectra of each observation were generated using `mkwarf`, and averaged weighted by the counts in each observation. The background was estimated from the spectrum of the particles that impacted the detectors during a 50 ks observation taken with the ACIS-I stowed out of the focal plane of the mirror assembly.

2.2. Millimeter Line Analysis

The ^{13}CO (1–0) data presented here were taken in 1993 April using the 15-element QUARRY focal plane array mounted at the Cassegrain focus of the 14-meter FCRAO telescope. Each pixel of the receiver employed a cooled Schottky diode mixer and 1.3–1.7 GHz HEMT IF amplifier. There was a common quasioptical single sideband filter with cooled image termination Erickson et al. (1992). The backend was a wideband filterbank spectrometer having 32 channels with 5 MHz (13.6 km s^{-1}) resolution for each pixel of the array.

Typical system temperatures referred to above the earth’s atmosphere were $\sim 800\text{--}1200$ K, the FWHM beam size was $\sim 50''$, and the main beam efficiency $\sim 40\%$. The ^{13}CO spectra were taken at 720 positions, with approximately one beam spacing, covering an area of $25' \times 20'$. The raw data were converted to CLASS format and the subsequent data reduction and analysis were carried out using the IRAM GILDAS software package.

2.3. Radio Continuum Analysis

The 20 cm images presented here are based on observations with the Very Large Array (VLA) of the National Radio Astronomy Observatory¹ observations that were carried out using B, C and D configurations. Details of data reductions are described in Yusef-Zadeh, Hewitt, & Cotton (2004). To measure the spectral index distribution, we compared the 20 cm image with a 90 cm image which was also based on multi-configuration observations with the VLA (Nord et al. 2004). The spatial frequency coverage of both 20 and 90 cm data were similar to each other so an accurate spectral index distribution could be determined. We convolved both images to a Gaussian having a FWHM= $12.6'' \times 12.6''$ before the spectral index image was constructed in AIPS. The rms noise for the two images are 3.6 and 2.5 mJy beam⁻¹ at 90 and 20 cm, respectively.

To search for polarized emission from Sgr C, we also reduced radio continuum observations of Sgr C at 3.6 and 2 cm which were observed in the DnC hybrid array configuration of the VLA in June 19, 1988. Standard calibration was done using NRAO530 and 3C286 as the phase and flux calibrators, respectively. The phase center for both pointings at 3.6 and 2 cm wavelengths is centered at $l=359^\circ 27' 14.04''$, $b=-2' 10.3''$. Based on 3.6 and 2 cm, we also placed a limit on the spectral index of the nonthermal filaments in Sgr C.

3. Results

We have compared the spatial distribution of X-ray, nonthermal radio continuum, molecular line and TeV emission and find a rough correspondence that suggests the they are related with each other. In particular, the analysis of the diffuse X-ray, molecular line and nonthermal radio continuum emission derive the iron flux, the column depth of molecular gas and the nonthermal particle flux. These basic observables are then used to measure how

¹The National Radio Astronomy Observatory is a facility of the National Science Foundation, operated under a cooperative agreement by Associated Universities, Inc.

cosmic rays interact with neutral material.

3.1. The Sgr C Molecular Complex

3.1.1. Diffuse X-ray Emission

Figure 1a shows contours of X-ray continuum emission from Sgr C between 2-6 keV. We note the evidence for several extended X-ray features in this H II complex. Diffuse features run vertically perpendicular to the Galactic plane, one of which is G359.42–0.12 with an extent of about $> 4'$ running to the south and the other is G359.45–0.07 with similar extent but appears clumpy as it runs to the north. Three relatively isolated and compact features are also found near G359.4–0.07, G359.32–0.16 and G359.46–0.15 with an extent of $\sim 1'$. These individual X-ray features will be discussed in §3.3 and §3.4.

We extracted an average X-ray spectrum of Sgr C from a region that enclosed the brightest parts of the diffuse and compact emission, as noted in Figure 1a, in the smoothed line images. We accounted for the background using the particle spectrum before we made the X-ray spectrum, as shown in Figure 1b. The extracted region is shown as an ellipse in a grayscale 6.4 keV EW image in Figure 2. The resulting spectrum of Sgr C, looks very similar to that of the diffuse emission analyzed by Muno et al. (2004a). The emission spectrum was modeled with a two-temperature plasma with and without a power-law component using the XSPEC spectral modeling package (Arnaud 1996). We assumed that each component was in collisional ionization equilibrium (the `apex` model in XSPEC), although the two components were not physically coupled (e.g., by conduction). We assumed that both components were absorbed by the same interstellar gas and dust, which we took to be distributed non-uniformly along the line of sight and across the image such that its effect could be described mathematically as

$$e^{-\sigma(E)N_H}([1 - f] + fe^{-\sigma(E)N_{pc,H}}). \quad (2)$$

Here $\sigma(E)$ is the energy-dependent absorption cross-section, N_H is the absorption column affecting the entire plasma, $N_{pc,H}$ is the column affecting part of the column, and f is the fraction of the plasma affected by $N_{pc,H}$. The parameters of the best-fit model are listed in Table 1.

The spectrum of the X-ray emission from Sgr C resembles that toward the inner 20 pc of the Galaxy, in that it can be modeled as plasma components with $kT_s \approx 0.5$ and $kT_h \approx 8$ keV (6). It is highly absorbed, with the column density toward $>97\%$ of the region reaching 10^{23} cm^{-2} , which is comparable to the total column depth of the molecular cloud. The derived emission measure of the soft plasma, $\int n_e n_H dl$ (Table 1), is highly dependent on the

absorption column, because a ≈ 0.5 keV plasma emits $< 1\%$ of its flux in the 2–8 keV band and photons below 2 keV are absorbed by the interstellar medium. Therefore, there is a factor of ~ 100 systematic uncertainty in the emission measure of the soft plasma, and our results cannot be compared easily to those using different absorption models. The emission measure of the hard plasma is less affected by absorption. We find a value of $1.0 \pm 0.1 \text{ cm}^{-6} \text{ pc}$ toward Sgr C, which is only a factor of two less than the average value of the inner 20 pc of the Galaxy (6).² Likewise, the intensity of the Fe K-alpha emission toward Sgr C is similar to that in the central 20 pc of the Galaxy, $\sim 1.2 \pm 0.1 \times 10^{-6} \text{ ph cm}^{-2} \text{ s}^{-1} \text{ arcmin}^{-2}$. The equivalent width of the Fe K- α line is $460 \pm 100 \text{ eV}$.

In the case where the spectrum was modeled by the inclusion of a power-law component, the fit is no better with a power law than without one. If we assume that the hot plasma producing the 6.7 keV iron lines has solar abundance, then up to 20% of the total de-absorbed 2–8 keV flux could be produced by a power law with the photon index Γ between 1 and 2. If we assume that the plasma has twice-solar iron abundance, then up to 45% of the flux could be produced by a non-thermal plasma. If larger abundances are assumed, as some Galactic center diffuse features such as the Arches and Quintuplet clusters indicate (e.g., Yusef-Zadeh et al. 2002; Law & Yusef-Zadeh 2004; Wang, Dong, & Lang 2006), it would imply that the line emission is accompanied by very little thermal continuum, so that the powerlaw can contribute yet more to the spectrum.

²We note that in Table 3 of Muno *et al.* (6), the emission measure is erroneously listed as being in units of $10^{-4} \text{ cm}^{-6} \text{ pc}$. It should actually be $\text{cm}^{-6} \text{ pc}$, as in Table 1 of this paper.

Table 1. Spectrum of the Diffuse X-ray Emission from Sgr C

Parameter	Value
$N_{\text{H},1}$ (10^{22} cm $^{-2}$)	$4.0^{+0.3}_{-0.1}$
$N_{\text{H,pc},1}$ (10^{22} cm $^{-2}$)	$10.7^{+0.5}_{-0.7}$
$f_{\text{pc},1}$	>0.97
kT_1 (keV)	0.5 ± 0.1
Z_1	0.3 ± 0.1
$K_{\text{em},1}$ (cm $^{-6}$ pc)	$231.5^{+79.2}_{-70.7}$
kT_2 (keV)	$7.6^{+1.0}_{-0.8}$
Z_2	0.6 ± 0.1
$K_{\text{em},2}$ (cm $^{-6}$ pc)	1.0 ± 0.1
$F_{\text{FeK}\alpha}$ (10^{-7} ph cm $^{-2}$ s $^{-1}$ arcmin $^{-1}$)	12 ± 1
χ^2/ν	335/325
$F_{\text{X},s}$ (10^{-14} erg cm $^{-2}$ s $^{-1}$ arcmin $^{-2}$)	3
$F_{\text{X},h}$ (10^{-14} erg cm $^{-2}$ s $^{-1}$ arcmin $^{-2}$)	9
$L_{\text{X},s}$ (10^{33} erg s $^{-1}$ arcmin $^{-2}$)	3
$L_{\text{X},h}$ (10^{33} erg s $^{-1}$ arcmin $^{-2}$)	2

^aParameter was not allowed to vary.

Note. — Uncertainties are 1σ , computed using $\Delta\chi^2 = 1.0$. The emission measure is defined as $K_{\text{em}} = \int n_e n_{\text{H}} dl$, where dl is the integral over the length in parsecs. Fluxes are observed values in the 2–8 keV band, and luminosities are computed from the de-reddened flux in the 2–8 keV band. The soft component emits $<1\%$ of its flux in the 2–8 keV band, so its emission measure could be lower by a factor of ≈ 100 if it is produced in a region with a lower column density than the hard emission.

3.1.2. X-ray and 20-cm Continuum Emission

Figure 3a,b show contours of X-ray continuum emission between 2-6 keV superimposed on two grayscale renditions of continuum emission from Sgr C at 20 cm. The 20 cm image shows the circular Sgr C H II region, as well as the prominent vertical structure which consists of bright nonthermal filaments running vertically toward more positive latitudes in the direction away from the Galactic plane. Figure 3c shows the same contours superimposed on a 90 cm image of the Sgr C region to present the relative distribution of nonthermal continuum and X-ray emission. Due to their steep spectrum, 90 cm continuum emission is generally a good tracer of nonthermal emission from synchrotron sources (Nord et al. 2004). We describe individual nonthermal radio filaments and argue that each radio filament has X-ray correspondence. The peaks of radio and X-ray features appear to be displaced between $15''$ and $60''$ with respect to each other. Five X-ray features are labeled in Figure 1a, all of which appear to be spatially correlated with the nonthermal radio continuum features, as each described below.

G359.45–0.07 One of the diffuse but clumpy X-ray features, G359.45–0.07, as labeled in Figure 1a, which runs along the brightest portion of the nonthermal radio filament of Sgr C. This nonthermal radio counterpart, labeled as RF-C1 (G359.45–0.06) in Yusef-Zadeh et al. (2004), is prominently detected at 90 cm (Nord et al. 2004).

G359.42–0.12 Another X-ray feature which appears to have a radio correspondence is G359.42–0.12 running parallel to a new vertical radio continuum feature. This new faint radio feature, as noted best in Figure 3b, extents for $8'$ with a typical surface brightness of ~ 10 mJy beam $^{-1}$. This radio continuum feature at $l=359^\circ 26'$ runs parallel to the eastern edge of the elongated X-ray feature G359.42–0.12. The centroid of the radio continuum and the X-ray continuum features is displaced by $\sim 1'$ in east-west direction.

G359.40–0.07 The third X-ray feature that appears to have a radio correspondence is G359.40–0.007 (Figs 3a,c). This X-ray feature lies at the northeastern edge of a filamentary radio feature which has been identified earlier at 20 cm (see RF-C14 (G359.32–0.06) in Yusef-Zadeh et al. 2004) and at 90 cm (Nord et al. 2004).

G359.46–0.15 Another X-ray feature G359.46–0.15 is noted at the southwestern edge of a long filamentary structure identified as RF-C4 (G359.49–0.12) at 20 cm (Yusef-Zadeh et al. 2004). Figure 3b shows the relative location of this faint X-ray emission with respect to the filament. An H II region (G359.47–0.17) lies to the south of the X-ray feature.

G359.32–0.16 Lastly, we notice in Figures 3a-c, a compact X-ray feature G359.32–0.16 which coincides with the brightest component of a nonthermal radio filament. This filament runs diagonally with a position angle of $\sim 60^\circ$ and is identified at 20 cm as RF-C13 in Yusef-Zadeh et al. (2004) and at 90 cm (Nord et al. 2004). High resolution radio continuum images show that the radio filament consists of multiple linear components running parallel to each other but peaking at the location of the X-ray feature G359.32–0.16. Figure 3d shows a close-up view of G359.32–0.16 where contours of X-ray emission are superimposed on a grayscale 20 cm continuum image. The distribution of X-ray emission is elongated along the direction of two parallel nonthermal radio filaments, suggesting that the X-ray and radio features could be associated with each other. Like other X-ray features that have radio continuum correspondence, a displacement of $\sim 15''$ is noted between the peaks of X-ray and radio emission. The displacement between nonthermal radio filaments and X-ray features is also seen in high-resolution images G0.11–0.08 (Yusef-Zadeh, Law, & Wardle 2002).

We extracted events from the isolated continuum X-ray feature G359.32–0.16. The events were selected from a $35.4'' \times 57.6''$ ellipse centered at $l=359.43382^\circ$, $b=-0.09655^\circ$ with radius $4.15'$ and $5.96'$ respectively, with a position angle (PA= 38.6°). The background was estimated using a local background. After accounting for the background, the region contains only 45 ± 16 net photons (90% uncertainty) in the *Chandra* band-pass, all of which lie between 3.3–8.0 keV; in the 0.5–2.0 keV band, there are <7 net counts, and in the 2.0–3.3 keV band there are <11 net counts. This does not provide enough signal to model the spectrum in detail. Therefore, following Munro et al. (2004b), we calculated a net photon flux of 1×10^{-7} photon $\text{cm}^{-2} \text{s}^{-1}$, and a hardness ratio $(h - s)/(h + s) = 0.2 \pm 0.4$, where h is the number of counts in the 4.7–8.0 keV band and s is the 3.3–4.7 keV band. If the absorption column to the source is $6 \times 10^{22} \text{ cm}^{-2}$, then we can use Figure 13 in Munro et al. (2004b) to estimate that the spectrum is consistent with a $\Gamma=1$ power law with a luminosity is $1 \times 10^{33} \text{ erg s}^{-1}$. Unlike other radio filaments in Sgr C, G359.32–0.16 does not seem to have a 6.4 keV correspondence, thus it is possible that this X-ray feature is an X-ray synchrotron source similar to other X-ray/radio nonthermal filaments that have been detected in the Galactic center region (Sakano et al. 2003; Lu, Wang & Lang 2003; Yusef-Zadeh et al. 2003).

In addition to radio filaments described above, Sgr C is surrounded by a number of additional weaker radio filaments that have been identified at 20 and 90 cm wavelengths (Nord et al. 2004; Yusef-Zadeh, Hewitt & Cotton 2004). We predict that a large-scale sensitive X-ray observations of this region with *Chandra* and *XMM-Newton* X-ray Observatories should detect additional X-ray correspondence to radio features.

3.1.3. ^{13}CO Line Emission

The ^{13}CO (1–0) emission in the vicinity of Sgr C spans a wide range of velocities, from approximately -200 to $+200$ km s^{-1} . Velocity channel maps in the -172 to 86 km s^{-1} range, where the brightest emission occurs, are shown in celestial coordinates in Figure 4. A number of distinct velocity components can be identified, some with velocities forbidden by the galactic rotation. The emission associated with the Sgr C molecular cloud is seen in the central part of the map in the -77 to -36 km s^{-1} channels. In addition, an elongated feature approximately parallel to the galactic plane is seen to the west of Sgr C at lower velocities (below -90 km s^{-1}). Another elongated feature, roughly perpendicular to the galactic plane, is seen in the north-east part of the map at velocities above -25 km s^{-1} .

Molecular column densities can be computed using eq. (8) of Lis & Goldsmith (1991) for a linear molecule:

$$N_{tot} = \frac{4.0 \times 10^{12} \text{ cm}^{-2}}{J^2 \mu^2 [\text{D}] B [\text{K}]} Z \exp\left(\frac{E_J [\text{K}]}{T_{ex}}\right) \times \frac{1}{\eta} \int T_A^* dv [\text{K kms}^{-1}] \quad (3)$$

In our case, $J = 1$, the dipole moment $\mu = 0.112$ D, the rotational constant $B = 2.64$ K, the partition function $Z = T_{ex}/B$, the upper level energy $E_1 = 2B$, and the main beam efficiency $\eta = 0.4$. Therefore

$$N_{tot} = 1.14 \times 10^{14} \text{ cm}^{-2} T_{ex} \exp\left(\frac{5.28}{T_{ex}}\right) \int T_A^* dv [\text{K kms}^{-1}] \quad (4)$$

The assumption of optically thin emission is justified given the relatively low ^{13}CO (1–0) line intensities compared to the peak line intensity observed in Sgr B2 (Lis & Goldsmith 1989). The dependence of the molecular column density on the excitation temperature is relatively mild, as the factor $T_{ex} \exp(5.28/T_{ex})$ varies between 21 and 46 for T_{ex} between 15 and 40 K. In the subsequent analysis we assume $T_{ex} = 25$ K (the cold component in the two-component gas model of Hüttemeister et al. 1993), and the fractional ^{13}CO abundance $X = 10^{-6}$, as determined for Sgr B2 (Lis & Goldsmith 1991), which gives

$$N_{\text{H}_2} = 3.5 \times 10^{21} \text{ cm}^{-2} \int T_A^* dv [\text{K kms}^{-1}] \quad (5)$$

The uncertainty in the molecular column densities is of order 40%, taking into account the uncertainties in the calibration and the excitation temperature.

The peak ^{13}CO (1–0) intensity integrated over the -200 to 200 km s^{-1} velocity range is

160 K km s⁻¹ and the average value over the area covered by our observations is 84 K km s⁻¹. The corresponding H₂ column densities are 5.6×10^{23} and 2.9×10^{23} cm⁻², respectively. Limiting the velocity range to -85 to -30 km s⁻¹, corresponding to the Sgr C cloud, results in the peak and average integrated line intensities of 80 and 22.3 K km s⁻¹, respectively. The corresponding H₂ column densities are 2.8×10^{23} and 8×10^{22} cm⁻², respectively. Assuming a distance of 8.5 kpc, the total H₂ mass contained within our map is 1.5×10^6 M_⊙ in the -200 to 200 km s⁻¹ velocity range and 4×10^5 M_⊙ in the -85 to -30 km s⁻¹ range. These values are much lower compared to the molecular mass of the Sgr B2 cloud $\sim 7 \times 10^6$ M_⊙ (Lis & Goldsmith 1989), in agreement with the general weakness of the ¹³CO emission in Sgr C compared to Sgr B2.

3.1.4. The Morphology of Fe K-α and ¹³CO Line Emission

Figure 5a shows contours of ¹³CO line emission integrated over the velocity range between -77 and -22 km s⁻¹ superimposed on the grayscale distribution of Fe K-α 6.4 keV line emission from Sgr C. The strongest molecular line emission has a velocity of -65 km s⁻¹ which identifies the Sgr C molecular cloud (Liszt & Spiker 1995). An isolated molecular feature near b $\sim -3'$ arises from the -120 to -90 km s⁻¹ molecular cloud. The strongest 6.4 keV line emission G359.48-0.15 arises from the western portion of the molecular cloud. The second strongest 6.4 keV peak emission is about 2' southwest of G359.48-0.15. These faint X-ray features are correlated better with the fainter lower velocity components near -40 km s⁻¹. It is clear that the overall distribution of the 6.4 keV emission follows the western edge of the -65 km s⁻¹ molecular cloud, as there is no X-ray emission from the eastern edge of the molecular cloud. Figure 5b shows another version of Figure 5a except that contours of ¹³CO emission are superimposed on the grayscale X-ray continuum emission. The continuum X-ray emission from the Sgr C complex is also consistent with being distributed to the western edge of the -65 km s⁻¹ molecular cloud. This suggests that the fluorescent 6.4 keV line emission and the X-ray continuum emission trace each other, though the line-to-continuum ratio may vary across the cloud. Moreover, the nonthermal filaments (see Figure 1 & 3) are detected only at the western edge of the Sgr C cloud. These images suggest the correspondence of Kα line and nonthermal radio emission at the western edge of the Sgr C molecular cloud.

We also note that distribution of the equivalent width of the Fe K-α line is strongest to the west of the -65 km s⁻¹ molecular cloud with a value of 450 eV. This peak coincides with the peak of ¹³CO emission at -65 km s⁻¹ at G359.47-0.15. Figure 5c shows contours of 2-6 keV X-ray emission superimposed on the 6.4 keV equivalent width image of Sgr C. The intensity of the Fe Kα line emission toward Sgr C is quite high, $\sim 6_{-4}^{+2} \times 10^{-6}$ ph cm⁻² s⁻¹

arcmin⁻², which is within at least a factor of ~ 2 larger than the average value in the central 20 pc of the Galactic center. Table 2 lists the parameters of the fit to the Sgr C region. The equivalent width of the Fe K- α line is not sensitive to the uncertainty introduced by the absorption.

The distribution of 6.4 keV line emission based on ASCA observations was compared with that of CS (1-0) line emission from Sgr C (Murakami et al. 2001a). However, the high negative velocity molecular gas with the velocity interval between -120 and -110 km s⁻¹ was compared with their low spatial resolution X-ray data. They assumed that the core of Sgr C is centered on the high negative velocity feature at -110 km s⁻¹. However, the core of Sgr C and the bulk of molecular gas is known to have a velocity of -65 km s⁻¹ (see Figure 5a,b), as a number of ionized and molecular studies have indicated (e.g., Tsuboi et al. 1991; Liszt & Spiker 1995; Lis & Carlstrom 1994). In order to make a more detailed comparison of our X-ray and radio continuum data with the -110 km s⁻¹ molecular feature, we used the same CS (1-0) molecular line data (Tsuboi et al. 1999) that Murakami et al. (2001a) had used. The distribution of ¹³CO is quite similar to CS(1-0) suggesting that both trace the overall molecular gas distribution in the region. Figures 6a, b show contours of CS(1-0) emission between -120 and -110 km s⁻¹ velocity interval superimposed on the 6.4 keV line and 90cm continuum distributions, respectively. We agree with Murakami et al. assessment that K α line emission at the position of l=359°26' lies at the edge of one of the CS peaks at this velocity interval. However, there is no evidence of strong K α emission counterpart to the CS peaks at positive galactic latitudes. Figure 6b shows that the nonthermal Sgr C filament lies also at the edge of the -110 km s⁻¹ velocity feature. The morphology of a nonthermal filament lying at the edge of K α -line emitting molecular gas is also made for the -110 km s⁻¹ velocity feature of Sgr C. Thus, the LECRs from the Sgr C filament could also be responsible for the origin of K α 6.4 keV line emission from the high negative velocity component, as discussed in more detail below. Thus, there are two issues that weaken the application of the irradiation model to the -110 km s⁻¹ cloud. One is that the ¹³CO integrated intensity in the -200 to 200 km/s velocity interval averaged over the area mapped is 84 Kkm/s. The corresponding value for the -120 to -110 km/s velocity range is 9.5 Kkm/s. One of the questions that arises is that the X-ray radiation nebula model would thus have to explain why only 11% of the molecular gas on the line of sight is irradiated assuming that the -110 and the -65 km s⁻¹ velocity components are part of the Sgr C cloud. The other is the lack of 6.4 keV emission from other peaks of the -110 km s⁻¹ cloud facing toward Sgr A*.

There is no X-ray counterpart to the edge of the cloud in our Chandra as well as XMM data when compared with Figure 1 of Murakami et al. (2001a). A number of reasons could be potentially responsible for this discrepancy. One is the low-resolution map based on their ASCA measurements which could be contaminated by point sources within 6.1-7 keV,

the there are not enough point sources to account for the excess emission. The other is their linewidth being different, 6.1-7.1 versus 5.8 to 7.0 keV. Lastly, time variability of the iron flux is also a possibility over the course of 8 years. However, the comparison of the iron flux from a knot-like feature at G359.48-0.15 with that of Murakami et al. (2001a) requires about 24 light years to explain the shift in the centroid of this knot-like feature. In addition, the derived EW (460 \pm 100) eV seems to be lower than the value (800 eV) obtained by Murakami et al. We believe the main reason for the difference is that we used different assumptions for the background emission. Murakami et al. (2001a) used an off-source region for the background, so their subtraction is both of particle background and (an estimate of) the Galactic diffuse emission. Our images were subtracted only by the particle background. Lastly, the excess emission could be due to a transient behind a cloud.

If the fractional ^{13}CO abundance in Sgr C is lower than in Sgr B2, the column density estimate could be higher. However, the $^{12}\text{C}/^{13}\text{C}$ ratio is ~ 20 in the Galactic center compared to the local value of 77 ± 7 (Wilson & Rood 1994). With $X(\text{CO})=10^{-4}$, the “nominal” Galactic center ^{13}CO abundance is $X(^{13}\text{CO})=4 \times 10^{-6}$. The low value of $X(^{13}\text{CO}) = 10^{-6}$ which we used is already low and is more consistent with the local ISM value (e.g., Frerking et al. 1982). This suggests that the estimated ^{13}CO abundance can not be lower.

Another useful method that traces the column density of molecular hydrogen is sub-millimeter emission. Figure 7 shows a grayscale 850 μm image of Sgr C based on SCUBA observations (Pierce-Price et al. 2000) and contours of ^{13}CO line emission. Two sub-millimeter peaks are noted; the northeastern component is a site of star forming region associated with the -65 km s^{-1} Sgr C cloud whereas the southeastern component is unlikely to be related to the Sgr C cloud. The peak sub-millimeter emission which lies in the vicinity of the peak of the molecular line emission has a flux density of 7.44 Jy per $15''^2$. The peak column density is then estimated to be $\sim 6 \times 10^{23} \text{ cm}^{-2}$ using the value of 513 $M_{\odot} \text{Jy}^{-1}$ at 850 μm , as derived by Pierce-Price et al. (2000). The mean value of the column density of the Sgr C cloud from sub-millimeter observations is about $2 \times 10^{23} \text{ cm}^{-2}$. This value is consistent with earlier estimates of the column density determined by Lis & Carlstrom 1994).

3.1.5. Spectral Index Measurements

We obtained a spectral index α (where flux density $F_{\nu} \propto \nu^{\alpha}$) distribution of Sgr C by using the 90 and 20 cm images (Nord et al. 2004; Yusef-Zadeh, Hewitt, & Cotton 2004), convolved with a FWHM Gaussian $12.6'' \times 12.6''$. Radio continuum emission from Sgr C at 90 cm is an excellent probe of nonthermal sources in this complex source. Figure 8a shows a slice cut of the spectral index distribution along the brightest filament whereas Figure

8b shows the error plot of the spectral index distribution. The spectral index is typically ranging between -1 ± 0.3 and -0.7 ± 0.1 to the south and to the north of the linear filament away from the Galactic plane, respectively. The emission from the Sgr C HII region at 20 cm is mainly responsible for the large error in the value of α to the south of the filament. These measurements are consistent with the spectral index values between -0.7 and -1 , as determined between 20 and 6 cm (Liszt & Spiker 1995). We also compared the 3.6 and 2 cm images of the bright nonthermal filament and found a steepening of the spectral index at shorter wavelengths.

Figures 9a,b show the 3.6 and 2 cm images, respectively, with a resolution of $6.8'' \times 6.4''$ (PA=10.2°). We note the vertical filament is detected prominently at 3.6 cm with a typical surface brightness of ~ 3 mJy beam $^{-1}$. However, the upper limit to the brightness of the filament is about 0.4 mJy beam $^{-1}$ at 2 cm. This filament was not detected at 1.2 cm either (Tsuboi et al. 1991). Accurate spectral index measurements restricting the uv range to 2 and 30 k λ for both the 3.6 and 2 cm data show that the spectral index of the bright filament is equal or steeper than -2.3 ± 0.5 . This suggests a break in the spectral index of nonthermal filaments from 90 to 2 cm, possibly due to the shorter lifetime of more relativistic particles at high energies. Previous spectral index measurements of other Galactic center filaments show similar spectral index break with a value of ~ -2 at shorter wavelengths than at 6 cm (Lang, Morris & Echevarria 1999). The first detection of polarized emission from Sgr C, as shown in Figure 10, is described in the Appendix.

3.2. Galactic Center Molecular Clouds at $l > 0^\circ$

3.2.1. 6.4 keV Emission

With the exception of the Sgr C molecular cloud that lies beyond Sgr A and at the negative longitude side of the Galactic center, the largest concentration of dense and warm molecular clouds is known to be distributed near Sgr A and in the positive longitude side of the Galactic center region (e.g., Morris & Serabyn 1996; Tsuboi, Handa & Ukita 1999). Four of the well-known molecular cloud complexes are “20 km s $^{-1}$ cloud” (M-0.13-0.05) distributed near Sgr A, the “45 km s $^{-1}$ cloud”, the “-30 km s $^{-1}$ cloud”, both of which extend between Sgr A and the radio arc at $l \sim 0.2^\circ$, and the molecular ridge extending from molecular cloud M0.25-0.01 to Sgr B2. The 45 and -30 km s $^{-1}$ clouds lie on one side of the radio arc and overlap with each other spatially. The largest concentration of bright and long nonthermal radio filaments are also found on the positive longitude side of the Galactic center (Yusef-Zadeh, Morris, & Chance 1984). The radio arc and its adjacent molecular clouds can potentially provide evidence for a mixture of interacting thermal and nonthermal

features. Given that relativistic particles of the Sgr C filaments are interacting with its molecular cloud, we believe that the interaction of nonthermal particles of the radio arc with its adjacent molecular clouds can also explain the nature of 6.4 keV emission, as described below.

To illustrate the proposed physical association between nonthermal radio filaments, the 45 and -30 km s⁻¹ molecular clouds and the 6.4 keV line emission, Figures 11a,b show grayscale views of the non-thermal radio filaments of the radio arc and Sgr A at 20 cm against the fluorescent 6.4 keV image and ammonia distribution (Güsten et al. 1981; Yusef-Zadeh 1986). Figure 11a shows the distribution of the K α EW line emission in green color and a 20 cm continuum image in red color whereas the NH₃(1,1) line emission from the “20 and 45 km s⁻¹ clouds” are displayed in Figure 11b as contours with a spatial resolution of 40". Given that ammonia line observations have lower resolution than radio continuum and X-ray observations, the overall distribution of bright knots of K α EW line emission correlate well with peaks of ammonia line emission associated with the “45” km s⁻¹ molecular cloud. We note that there is no evidence for strong compact or diffuse K α line emission from the “20 km s⁻¹ cloud”. This cloud is one of the most prominent dust continuum features in the Galactic center showing high mass and column density. Furthermore, nonthermal filaments have been detected toward this cloud. Similarly, another massive cloud that shows a lack of EW of K α line emission is M+0.25+0.01. Individual compact ammonia clumps of the 45 km s⁻¹ molecular cloud that have 6.4 keV line correspondence, as shown in Figure 11b, are M0.06–0.04, M0.10–0.01, M0.11–0.08, M–0.02–0.07 and M0.07–0.08 (e.g., Serabyn & Güsten 1987; Lang, Goss, & Morris 2002). The molecular clump M0.11–0.08 lies closest in projection to the nonthermal filaments of the arc has been extensively mapped recently in CS, SiO and H¹³CO⁺ lines. This clump has velocities ranging between 15 and 45 km s⁻¹ and has a strong 6.4 keV line counterpart (Tsuboi, Ukita, & Handa 1997; Yusef-Zadeh, Law, & Wardle 2002; Handa et al. 2006).

Another cloud that is dynamically coupled to the thermal component of radio arc is the -30 km s⁻¹ cloud (Serabyn & Güsten 1987). This cloud is distributed on the positive latitude side of the arc and is associated with thermal gas of the arched filaments which is ionized by the Arches cluster G0.121+0.017 (e.g., Cotera et al. 1996; Figer et al. 1999; Lang, Goss & Morris 2002). The comparison of the distributions of the CS molecular gas and K α line emission suggests that the K α line peaks follow the distribution of the CS emission (Serabyn & Güsten 1987). In fact, one of the ammonia peaks M–0.02–0.05 (–15 km s⁻¹), as shown in Figure 11b, coincides with a southern extent of the -30 km s⁻¹ molecular cloud. M–0.02–0.05, as well as the CS peaks 1 and 2 identified by Serabyn & Güsten (1987) have 6.4 keV line correspondence. Lastly, another knot-like K α line emission G0.12+0.00 distributed in the immediate vicinity of Arches cluster G0.121+0.017 appears to be associated with a CS

molecular emission (Lang, Good & Morris 2002; Serabyn & Güsten 1987).

The hook-shaped structure noted in the the $K\alpha$ EW line distribution correlates extremely well with the ammonia distribution, as noted in Figures 11a,b. In addition to non-thermal emission from magnetized filaments and the recent detection of nonthermal emission from the Arches cluster provide another source for the interaction of cosmic rays with molecular gas to explain the origin of the 6.4 keV line emission. Although the total mass of molecular gas and radio continuum flux of nonthermal emission in the arc region are much higher than that those in Sgr C, the column density of molecular gas and the EW of $K\alpha$ line of about few hundred eV are similar to those of Sgr C. With the exception of G0.11–0.08 molecular cloud which is closest to the filaments in projection having a hydrogen column density of $7\text{--}8 \times 10^{23} \text{ cm}^{-2}$, the peaks of the 45 km s^{-1} and -30 km s^{-1} clouds show column densities of of few times 10^{23} cm^{-2} (Güsten et al. 1981; Serabyn & Güsten 1997). The density and temperature of molecular gas from these clouds are also estimated to be about $\text{few} \times 10^4 \text{ cm}^{-3}$ and 50–80 K, respectively.

In the context of low-energy cosmic ray model, these characteristics imply that cosmic ray particles penetrating molecular clouds should be uniform with similar metallicity as discussed in more detail in §4.2 We measured the $K\alpha$ line and continuum X-ray flux of the arc by taking a spectrum over an area of 123 arcmin^2 encompassing both 45 and -30 km s^{-1} molecular clouds. An absorbed power-law plus Gaussians were used to model all of the line emission. This model is not physically motivated, but allows to measure fluxes and equivalent widths. The de-reddened continuum flux between 2–8 keV, Fe $K\alpha$ EW and Fe $K\alpha$ flux are $5.6 \times 10^{-11} \text{ erg cm}^{-2} \text{ s}^{-1}$, 670 eV and $3.5 \times 10^{-4} \text{ ph cm}^{-2} \text{ s}^{-1}$, respectively. The parameters of the fits to Sgr C, the radio arc, Sgr B1 and Sgr B2 are shown in Table 2. These parameters are derived assuming a model of a power-law continuum under which the absorption columns are estimated to be lower than in thermal plasma models by a factor of 2–3. This results in a 30% lower estimated flux for the line from Sgr C, which should be taken as the systematic uncertainty in the measurement.

Table 2. Parameters of X-ray Fit to Galactic Center Clouds

Region	Area (arcmin ²)	Fe K α Flux (ph cm ⁻² s ⁻¹)	Fe K α EW (eV)	Flux (2–8 keV) (erg cm ⁻² s ⁻¹)	De-reddened Flux (erg cm ⁻² s ⁻¹)
Sgr C	77	$7.2(0.2) \times 10^{-5}$	470(100)	$9.1(0.1) \times 10^{-12}$	$1.2(0.2) \times 10^{-11}$
Radio Arc	123	$3.5(0.1) \times 10^{-4}$	670(50)	$3.7(0.1) \times 10^{-11}$	$5.6(0.1) \times 10^{-11}$
Arches Cluster	1.6	$1.3(0.1) \times 10^{-5}$	810(200)	$9.1(0.1) \times 10^{-13}$	$1.2(0.2) \times 10^{-12}$
Sgr B1	77	$8.6(4) \times 10^{-5}$	570(70)	$7.6(0.1) \times 10^{-12}$	$9.7(0.7) \times 10^{-12}$
Sgr B2	96	$2.4(0.1) \times 10^{-4}$	1150(150)	$9.5(0.1) \times 10^{-12}$	$1.1(0.1) \times 10^{-11}$

To examine the impact of low-energy cosmic ray particles with molecular gas throughout the Galactic center, we also list in Table 2 the fitted parameters to two other Galactic center molecular cloud complexes Sgr B1 and B2. These clouds are associated with the molecular ridge that extends between G0.25+0.01 and Sgr B2, as shown in Figure 2. Both these clouds have been extensively studied in millimeter and submillimeter wavelengths, as well as in $K\alpha$ line (e.g., Hüttemeister et al. 1993a; Lis & Carlstrom 1994; Murakami et al. 2001). The regions from which spectra were extracted from Sgr C, the radio arc, Sgr B1 and Sgr B2 are drawn on a large-scale 6.4 keV EW line distribution, as displayed in Figure 2. A more detailed study of the individual 6.4 keV line features will be given elsewhere.

3.2.2. *TeV Emission*

Recent observation with HESS has discovered large-scale diffuse TeV emission from the inner 200 pc of the Galaxy (Aharonian et al. 2006). The morphology of diffuse emission correlates well with the distribution of CS molecular clouds, thus suggesting that the γ -ray emission is a product of the interaction of cosmic rays with interstellar gas near the Galactic center. These authors show that the spectrum of TeV emission from resolved clouds toward the Galactic center has a photon index $\Gamma \sim 2.3$ which is harder than in that in the Galactic disk. They note that the γ -ray flux above 1 TeV is a factor of 3-9 times higher than in the Galactic disk and argue for an additional population of cosmic rays in this unique region. They propose that the TeV emission is due to hadronic interaction of cosmic rays with the target material. Their argument against the importance of TeV electrons is the short lifetime of their energies.

Given that the target material is the same, we compared the distribution of TeV emission with that of the 6.4 keV emission from molecular gas toward the Galactic center. Figure 12a shows contours of diffuse TeV emission superimposed on a grayscale image of $K\alpha$ 6.4 keV line emission. The prominent TeV peaks are seen toward Sgr C, the radio arc and Sgr B. Due to the subtraction of the compact and bright source coincident with Sgr A*, it is not clear if the weak feature near G359.83–0.1 is real or due to an artifact of subtraction (J. Hinton, private communication). As expected, there is a strong concentration of 6.4 keV knots which correlates well with the peaks of TeV emission toward Sgr C, Sgr B and the arc. The brightest TeV emission from diffuse galactic center molecular clouds is detected toward the radio arc followed by Sgr B2 and Sgr C. We also note that both the TeV and $K\alpha$ line emissions from the well-known “20 km s^{–1}” molecular cloud G–0.13–0.08 are weak. To illustrate the relationship between molecular gas, nonthermal filaments and the fluorescent line emission, Figure 12b shows the contour distribution of submillimeter emission distributed against a

20 cm continuum emission (in green) and 6.4 keV emission (in red). All the prominent molecular clouds are represented in the submillimeter image.

4. Discussion

There are three different types of observations that are used in support of large-scale high energy activity in the inner few hundred pcs the Galactic center. These observations suggest that this activity is more pronounced than that observed in the disk of the Galaxy for the following reasons. One is the distribution of nonthermal radio emission traced by magnetized radio filaments, a 1° scale diffuse structure, known as the Galactic center lobe, a high concentration of confirmed supernova remnants such as G0.0+0.0 or Sgr A East (Ekers et al. 1983), G0.3+0.0 (Kassim & Frail 1996), G0.9+0.1 (Helfand & Becker 1987), G1.0-0.1 or Sgr D (Downes et al. 1979) and G359.1 -0.5 (Downes et al. 1979) as well as nonthermal emission from colliding winds of massive stars in dense stellar clusters. These sources, altogether signify regions of enhanced synchrotron emissivity (e.g., Gray 1994; Nord et al. 2004; Yusef-Zadeh et al. 2004; Law 2006). The recent detection of diffuse low-frequency radio continuum emission (LaRosa et al. 2006), as well as other indirect measurements (Yusef-Zadeh 2003) suggest that the large-scale diffuse distribution of the magnetic field can not be too different than that observed in the Galactic disk. This is consistent with the picture that the Galactic center nonthermal radio filaments are expected to have a stronger magnetic field than that of the surrounding diffuse and weakly magnetized medium. Recent interpretation of the nonthermal filaments suggests that kinematic dynamo enhances the magnetic field in a medium which is initially threaded by weak magnetic field (Bodyrev & Yusef-Zadeh 2006). Thus, we suggest that cosmic ray electron density of the diffuse gas must be enhanced in the Galactic center region in order to account for the excess synchrotron emissivity detected toward the central 200 pcs of the Galaxy. Another recent measurements come from H_3^+ and H_3O^+ observations suggesting that the ionization rate due to cosmic rays has to be higher by one to two orders of magnitude in the Galactic center region than in the disk (Oka et al. 2005; van der Tak et al. 2006). Lastly, the recent discovery of diffuse TeV emission from the Galactic center molecular clouds shows enhanced γ -ray emission at higher energies having a spectrum that differs from that of the cosmic rays in the disk of the Galaxy.

Table 3. Parameters of the LECR Model

Region	Area (arcmin ²)	90 cm Flux (Jy)	Energy Density (eV cm ⁻³)	Magnetic Field (mG)	spectral index (α)
Sgr C	0.024	0.05	1200	0.22	-0.7
Radio Arc	285	260	19	0.029	0.0
Arches Cluster	1.6	0.36	6×10^4	1.6	-1
Sgr B1	77	3.2	23	0.03	-0.7
Sgr B2	96	18	51	0.045	-0.7

Based on the above arguments, it is natural to consider the possibility that enhanced cosmic rays in the Galactic center region could play an important role in accounting for much of the observed high energy activity in this region. This hypothesis stem from the fact that a great deal of warm and dense molecular gas is distributed in the central region (e.g., Rodriguez-Fernandez et al. 2001), thus, the widely distributed molecular gas can be used as an excellent target by the impact of enhanced cosmic rays. In particular, the origin of the observed 6.4 keV emission throughout the Galactic center region can be tied to the impact of low-energy cosmic ray electrons with molecular gas. The role of low-energy cosmic rays was first proposed to explain the origin of the Galactic X-ray ridge (Valinia et al. 2002). This model was subsequently applied to G0.11–0.08 (Yusef-Zadeh, Law, & Wardle 2002). We argue below that this model can also be applied to Sgr C, as well as other Galactic center molecular clouds. In addition, we argue an alternative model to explain the origin of TeV emission from molecular clouds near the Galactic center. We suggest that the high-energy component of electrons can potentially be responsible to inverse Compton scatter the intense submillimeter emission to account for the origin of γ -ray emission.

4.1. The Irradiation versus LECRs Model

One of the main results of our analysis of the millimeter and X-ray data is that the distributions of the 6.4 keV line and 2-6 keV continuum emission arise from the western edge of the ^{13}CO molecular cloud. The main body of the Sgr C cloud does not show any evidence of X-ray emission except from its western edge which faces away from the direction of Sgr A*. The origin of fluorescent line emission resulting from irradiation by a hypothetical transient source associated with Sgr A* has been applied to the Galactic center molecular clouds (e.g., Sunyaev, Markovitch, & Pavlinsky 1993; Koyama et al. 1996; Murakami et al. 2001a; Park et al. 2004). However, unlike Sgr B2, the X-ray emission from Sgr C faces away from the suggested illuminating source, Sgr A*. The column density of molecular hydrogen $10^{23} - 10^{24}$ correspond to Thompson optical depth τ_T of 0.1 to 1 (Sunyaev & Churazov 1998). If the illuminating source is outside the cloud, the expected equivalent width (EW) exceeds 1 keV for an optically thin or thick case. The combined distribution of 6.4 keV line emission from Sgr C with respect to the bulk of molecular gas as well as Sgr A* when combined with the estimated EW of ~ 470 eV toward Sgr C suggest strongly that the irradiation model is unlikely to be applicable to Sgr C.

We propose an alternative model to explain the origin of X-ray emission from Sgr C in terms of the impact of low energy cosmic rays (LECRs) with molecular gas. The motivation for such a process stems from the fact that Sgr C is surrounded by a large concentration of

nonthermal radio emission associated with radio filaments. Given that the centroids of X-ray and radio continuum features are displaced with respect to each other, it is remarkable that all the X-ray continuum features, labeled in Figure 1a, appear to be located in the vicinity of peak nonthermal radio continuum emitting features associated with the Sgr C nonthermal filaments. Furthermore, the 6.4 keV line emission generally follows the X-ray continuum emission for almost all the X-ray features with the exception of G359.32–0.16 which could be a pure nonthermal continuum source with no X-ray emission lines or molecular counterpart. The model proposed here can naturally explain the origin of hot molecular gas observed throughout the Galactic center molecular clouds.

In the context of LECR model, the remarkable mixture of thermal and nonthermal radio components in Sgr C can produce not only the 6.4 keV line emission but also the nonthermal bremsstrahlung emission from Sgr C. As pointed out in §2, the X-ray spectrum could be equally fitted by a combined soft thermal and a power-law spectrum as long as the metallicity is higher than solar value. The power-law spectrum of the continuum emission from Sgr C is consistent with the LECR model, as described quantitatively below.

What about nonthermal filaments that have X-ray counterparts with no 6.4 keV counterpart? We believe that a flat spectrum of these filaments reduces the number of low energy cosmic rays for interaction with molecular gas but increases the number of high energy particles needed to produce synchrotron X-ray emission. The nonthermal X-ray filament discovered by Sakano et al. (2003) coincides exactly with a flat nonthermal radio source which is thought to be associated with “the 20 km s^{−1} molecular cloud” (Ho et al. 1985; Coil & Ho 2000; Yusef-Zadeh et al. 2005). Assuming that this cloud is near the Galactic center, the lack of strong 6.4 keV and TeV emission from this molecular cloud could be explained by the flat spectrum of its nonthermal filament.

The source of the enhanced cosmic-ray electrons is acceleration at the interaction site between the Sgr C molecular cloud and the Sgr C nonthermal radio filaments. The distribution of diffuse and filamentary X-ray gas lying at the edge of the filaments imply the presence of relativistic electrons in the vicinity of the diffuse X-ray source. However, the X-ray and radio features, as identified in Figures 1a and 3, are either displaced from each other or the X-ray features peak at the edge of nonthermal radio filaments. A displacement was also observed between the peak emission from radio filaments of the continuum arc and the M0.11–0.08 molecular cloud. The filaments of the arc and G0.11–0.08 are thought to be interacting with each other (Tsuboi et al. 1997; Oka et al. 2001). In addition, LECR model has been successfully applied to this cloud (Yusef-Zadeh, Law, & Wardle 2002). So, the displacement of radio emitting filaments and molecular cloud may be widespread in clouds that are interacting with nonthermal radio filaments. We believe this characteris-

tic can be explained by the geometry of the interacting non-thermal filaments with respect to the distribution of the molecular cloud. As described below, the low-energy relativistic particles interacting with neutral gas lose energy much more than the GeV particles that produce radio emission at high frequencies. The high-energy particles could be oblivious to the presence of molecular gas in their vicinity.

Interaction of cosmic rays with molecular gas has recently been argued to explain the origin of TeV emission from diffuse molecular gas. The grayscale image in Figure 12 shows contours of TeV emission from the Galactic center region superimposed on a large-scale distribution of Fe K α line EW emission. There appears to be a correlation between the 6.4 keV EW line emission and TeV emission. The strongest TeV emission arises from the region near the arc which is coincident with an EGRET source, as well as a soft γ -ray source 1743.1-2843 detected with INTEGRAL between 50 and 100 keV (Belanger et al. 2006). This source has been suggested to be produced as a result of the impact of GeV particles of the nonthermal filaments and G0.11–0.08 (Yusef-Zadeh, Law, & Wardle 2002). Whatever the mechanism responsible for the γ -ray emission from this source, it is suggestive that cosmic rays interacting with dense Galactic center molecular clouds are responsible for both types of X-ray, as well as soft and hard γ -ray emission. Apart from supernova remnants and nonthermal filaments, massive stellar clusters can also provide relativistic particles generated as a result of wind-wind collision in a dense stellar cluster. The Arches cluster is one example that has shown a flux of ~ 100 mJy of nonthermal emission from the cluster (Yusef-Zadeh et al. 2003).

4.2. Injection of Cosmic Rays into Molecular Clouds

We now calculate production rate of Fe K α photons associated with the injection of $dn(E)/dt$ electrons per unit energy interval per unit time into a cloud with column density N_H . The column density of the Sgr C cloud in the vicinity of the X-ray emission is $N_H \sim 10^{23} \text{ cm}^{-2}$. This is sufficient to stop electrons with energies below ~ 1 MeV; the rapid increase in penetrating power with energy means that higher energies pass through this column with little fractional energy loss (see, e.g. ICRU 1984). Electrons with initial energy below a critical value $E_c(N_H)$ (1 MeV for 10^{23} cm^{-2}) are stopped in the cloud. A single electron injected with energy $E < E_c$ produces

$$z\omega_K f_\alpha \int_0^E \sigma_K(E') \frac{-dN_s}{dE'} dE' \quad (6)$$

Fe K α photons while coming to rest, where z is the abundance of iron relative to hydrogen ($z_\odot = 2.8 \times 10^{-5}$), $\omega_K = 0.342$ is the fraction of K-shell ionizations that produce

K-characteristic X-rays, $f_\alpha = 0.822$ is the fraction of those that produce a $K\alpha$ photon, and $N_s(E)$ is the column density traversed by electrons of initial energy E before coming to rest. In steady state the net $K\alpha$ production rate produced by the injected electrons with energies $E < E_c$ is therefore

$$Q_1 = z\omega_K f_\alpha \int_0^{E_c} \frac{dn(E)}{dt} \int_0^E \sigma_K(E') \frac{-dN_s}{dE'} dE' dE. \quad (7)$$

Reversing the order of integration yields

$$Q_1 = z\omega_K f_\alpha \int_0^{E_c} \sigma_K(E) \frac{-dN_s}{dE} \frac{dn}{dt}(E < E' < E_c) dE. \quad (8)$$

Electrons that enter the cloud at higher energies only lose a fraction of their energy; for simplicity we neglect this energy loss in calculating their contribution to the Fe $K\alpha$ production rate, and write:

$$Q_2 = z\omega_K f_\alpha N_H \int_{E_c}^{\infty} \frac{dn}{dt}(E) \sigma_K(E) dE. \quad (9)$$

This “thin-target” approximation is adequate for our purposes here because σ_K varies by only a factor of two between 10 keV (e.g. Tatischeff 2003) and 1 GeV.

For $\sigma_K(E)$ we use the semi-empirical expression of Quarles (1976) with an ionization threshold energy $I = 7.1$ keV appropriate for neutral or almost-neutral iron. The spectrum of injected electrons is assumed to be a power-law (E^{-p}) between 10 keV and 1 GeV, normalized so that the corresponding power is 1 erg/s. The corresponding production rate $q = Q_1 + Q_2$ of Fe $K\alpha$ photons per erg of injected electron energy is calculated using eqs (8) and (9) as a function of cloud column density.

The results are plotted in Figure 13a for electron spectral indices p ranging from 2 to 3 and a solar iron abundance. For a given particle spectral index p , the efficiency of $K\alpha$ production increases with column density, eventually flattening when the column is sufficient to stop the bulk of the injected electrons within the cloud. For the $p = 2$ injection spectrum, which has equal energy per decade between 10 keV and 1 GeV, this occurs above 10^{25} cm^{-2} , which can only stop electrons with energies below 0.1 GeV. Steeper spectra have particle energies increasingly concentrated towards 10 keV and so the flattening of the $K\alpha$ production rate occurs at successively lower column densities. These results are consistent with those of Tatischeff (2003) who found $q \sim 50 \text{ ph erg}^{-1}$ for 10–100 keV electrons with an E^{-2} spectrum. We conclude from Figure 13a that typically $q \sim 50 z/z_\odot \text{ ph erg}^{-1}$ for typical spectral indices and cloud column densities, increasing to $\sim 100 z/z_\odot$ for hard electron spectra and high column densities. The bremsstrahlung emission at 6.4 keV was estimated

similarly; the resulting equivalent width is plotted in Fig. 13b. For $z = z_\odot$, the equivalent width varies between 250 and 300 eV for particle spectral index p varying between 3 and 2. There is little dependence on column except for p close to 2 and columns in excess of 10^{24} cm^{-2} , where the equivalent width increases from 300 to 340 eV as the column increases towards 10^{25} cm^{-2} . The Galactic center molecular clouds have typical metallicity that is on the average twice the solar value (e.g., Giveon et al. 2002; Rudolph et al. 2006). Thus, the production of $\text{K}\alpha$ line emission per erg of energy and the EW of $\text{K}\alpha$ emission, as shown in Figure 13, should be increased by a factor of two when applied to the Galactic center molecular clouds.

4.3. Application of Low Energy Cosmic Ray Model

To estimate the flux of electrons into the cloud, we assume that they diffuse from their acceleration site to the cloud edge, and then freely stream into the cloud because ion-neutral damping suppresses the magnetic fluctuations responsible for the diffusion. If the energy density of the electrons external to the cloud is U , then the flux into the cloud is $\sim cU/4$, giving an injection rate $cUA/4$ where $A \sim \Omega d^2$ is the cloud surface area impinged upon by electrons, Ω is the solid angle of the X-ray emission and d is the distance to the cloud from the Earth. The production rate of Fe $\text{K}\alpha$ photons is $Q \approx cU\Omega d^2 q/4$. The intensity of Fe $\text{K}\alpha$ photons at the Earth is then

$$I_{\text{K}\alpha} = \frac{Q}{4\pi d^2 \Omega} = \frac{cUq}{16\pi} \approx 8 \times 10^{-6} \left(\frac{U}{10^3 \text{ eV cm}^{-3}} \right) \left(\frac{z}{2z_\odot} \right) \text{ ph s}^{-1} \text{ cm}^{-2} \text{ arcmin}^{-2} \quad (10)$$

comparable to the observed peak Fe $\text{K}\alpha$ intensities if $U \sim 1000 \text{ eV cm}^{-3}$.

We apply this model to some of the sources in the Galactic centre region. In each case we assume that the nonthermal radio emission is produced by a power-law spectrum $n(E) \propto E^{-p}$ of electron energies between 10 keV and 1 GeV, assume that the depth of the emitting region is of the order of its diameter and calculate the energy density of cosmic-ray electrons assuming that they are in equipartition with the magnetic field. Eq. (10) is then used to compute the predicted Fe $\text{K}\alpha$ flux; when the source of particles is assumed to be either embedded within the cloud or completely surrounds it this estimate is increased by a factor of 4 to allow for the increase in exposed surface area exposed to the incident cosmic rays (ie. $4\pi r^2$ rather than πr^2). Note that although the incident electron spectrum may deviate from a power law below 100 keV because of ionization losses, this is not a major uncertainty as these electrons contribute $\lesssim 20\%$ of the $\text{K}\alpha$ flux. The model parameters needed to match the observed quantities for each source are listed in Table 3.

4.3.1. *Sgr C*

The brightest filament associated with Sgr C has a typical synchrotron flux at 90 cm of 50 mJy per $12.6'' \times 6.8''$ beam with a $\nu^{-0.7}$ spectrum. This is a lower limit to the flux of synchrotron emission because diffuse synchrotron emission, free-free absorption by intervening thermal gas, as well as contribution from weak nonthermal filaments have not been accounted for. The equipartition field is 0.22 mG with an electron energy density of 1200 eV cm^{-3} . This implies a peak $K\alpha$ flux of $9.7 \times 10^{-6} \text{ ph cm}^{-2} \text{ arcmin}^{-2}$ which is about 1.5 times that observed. We have used a particle spectral index $p = 2.4$ (where $n(E) \propto E^{-p}$) and equipartition between electrons and magnetic field. The measured spectral index values between 90 and 20 cm wavelengths agree well with the energy density in relativistic electrons required to match the synchrotron emission.

4.3.2. *The 45 and -30 km s⁻¹ clouds near the Radio Arc*

The filaments of the radio arc has a flux of $\sim 28 \text{ Jy}$ at 90 cm over its $3' \times 20'$ area, with a $\nu^{-0.5}$ spectrum. This spectrum is consistent with that measured between 408 and 160 MHz (Yusef-Zadeh et al. 1986). Most of the diffuse nonthermal emission is likely to be resolved out so we used the Green Bank observations of this region (Law et al. 2006) and measured a total integrated flux of 200 Jy over $285''^2$. This region includes the linear filaments of radio arc as well as other weaker nonthermal filaments that have recently been discovered (Reich 2003; Yusef-Zadeh et al. 2004; Nord et al. 2004) within the area of the extracted X-ray spectrum (Figure 11 and the box area in Figure 2). Due to the contamination by thermal H II features, as well as the background emission at 90 cm, the flux of nonthermal emission has a large uncertainty. Using the recent 20 cm continuum image which includes the zero spacing flux (Yusef-Zadeh et al. 2004), we found a similar flux of about 200 Jy which is consistent with the 90 cm measurements having a flat spectral index between 20 and 90 cm (Yusef-Zadeh et al. 1986).

Adopting 28 Jy of flux density of the nonthermal filaments of the arc at 90 cm and assuming that the arc consists of filaments of thickness $30''$, then the equipartition field is 0.07 mG and the energy density of electrons is 110 eV cm^{-3} . The predicted $K\alpha$ flux, $4 \times 10^{-5} \text{ ph cm}^{-2} \text{ s}^{-1}$, is much lower than that measured ($3.5 \times 10^{-4} \text{ ph cm}^{-2} \text{ s}^{-1}$). If we assume instead that the source is embedded in a diffuse distribution of low-energy cosmic-ray electrons over 285 arcmin^2 with a source depth of $15'$, then we find that an energy density of 38 eV cm^{-3} is required, with field strength 0.039 mG and synchrotron flux of 860 Jy. If the column density of the clouds is $\sim 10^{24} \text{ cm}^{-2}$ and $p \sim 2$ then q increases to $100z/z_{\odot} \text{ ph erg}^{-1}$; the required energy density, field strength and diffuse synchrotron flux are reduced to 19

eV cm^{-3} , 0.0289 mG and 260 Jy respectively.

4.3.3. *The Arches Cluster*

As discussed §3.2, we found a knot-like $\text{K}\alpha$ emission in the vicinity of the arches cluster. The source of cosmic ray particles injecting into the cloud surrounding the Arches cluster can either be the nonthermal filaments of the arc or nonthermal particles generated by cluster. Figure 14 shows a detailed view of the arches cluster which coincides with a compact nonthermal radio continuum source (in dark) at 90 cm (Yusef-Zadeh et al. 2003) against the grayscale distribution of the EW of 6.4 keV line emission. An X-ray spectrum was extracted from the region shown in Figure 14 which roughly encloses the 600 eV contours. The extracted region, as shown in Figure 2, is defined by an ellipse centered on $l=7^{\circ}33.7''$, $b=1^{\circ}08.6''$ having a major and minor axis of $62.7''$ and $29.1''$ ($\text{PA}=25^{\circ}$), respectively. The parameters of the iron line emission are shown in Table 2 having $\text{Fe K}\alpha$ EW of 810 eV . The peak EW emission in Figure 14 is as much as 1000 eV .

The nonthermal 327 MHz flux from the arches cluster is 91 mJy over a $7''$ by $13.5''$ region (Yusef-Zadeh et al. 2002), with a spectral index $\alpha \approx 1$ (for $S\nu \propto \nu^{-\alpha}$). The equipartition magnetic field is 1.1 mG and the energy density of electrons is $3 \times 10^4 \text{ eV cm}^{-3}$. The predicted $\text{K}\alpha$ flux, $6.5 \times 10^{-6} \text{ ph cm}^{-2} \text{ s}^{-1}$, agrees with that observed by Wang et al. (2006), i.e. $6.2 \times 10^{-6} \text{ ph cm}^{-2} \text{ s}^{-1}$. However, if we use the integrated $\text{K}\alpha$ flux from the region shown in Figure 14 and Table 2, the required 90 cm flux increases to 360 mJy of nonthermal emission from the arches cluster with an equipartition magnetic field of 1.6 mG . The additional flux of nonthermal emission must arise from the diffuse nonthermal emission surrounding the cluster or the emission from the nonthermal filaments of the arc.

4.3.4. *Sgr B2 and Sgr B1*

Radio continuum observations of the Sgr B complex shows two major components Sgr B1 (G0.5–0.0) and Sgr B2 (G0.7–0.0), as well as an intervening source G0.6–0.0 in the middle of these extended H II regions. (e.g., Mehringer et al. 1992). Diffuse thermal emission dominates Sgr B1 whereas numerous ultracompact H II regions overwhelm the emission in Sgr B2.

The continuum emission from Sgr B2 is mainly due to several dozen ultracompact H II regions and there is no known source of nonthermal filaments in its vicinity. However, there is a bright compact radio source detected at 90 cm with a flux density of 112 mJy

at $l=40' 2.1''$, $b=-2'7''$ detected at 90 cm (Nord et al. 2004). This source is likely to be nonthermal due to colliding winds from binary systems similar to the bright nonthermal source in the Arches cluster (Yusef-Zadeh et al. 2007, in preparation). If we assume that this central nonthermal radio source has a size about $10'' \times 10''$ with $\nu^{-0.7}$ spectrum, the equipartition field is 0.36 mG with an electron energy density of 2500 eV cm^{-3} is estimated. This also yields an estimated flux of $3.3 \times 10^{-6} \text{ ph cm}^{-2} \text{ s}^{-1}$ assuming $q = 150 \text{ ph erg}^{-1}$. In light of its large column density and including a factor of 4 leakage from the nonthermal source because it is entirely enclosed within the molecular cloud (so the relevant surface area is $4\pi r^2$ rather than πr^2), the predicted flux is still 50 times lower than observed. Another difficulty is that strength of the equivalent width of $K\alpha$ line emission is roughly two times higher than other Galactic center clouds with the exception of the Arches cluster.

Thus, the lack of strong localized nonthermal emission (unlike other galactic center molecular clouds) makes it difficult to apply the LECR picture to Sgr B2. However, the strong three-way correlation between the distribution of molecular clouds, the $K\alpha$ line emission and TeV emission from the Galactic center clouds suggest that the same process should be able to explain these observations. Adopting a size of 96 arcmin^2 , source depth $10'$, and a $\nu^{-0.7}$ spectrum, the required electron energy density, equipartition field and resulting 90 cm synchrotron flux are 51 eV cm^{-3} , 0.045 mG and 18 Jy respectively. Observationally, there may be diffuse nonthermal emission surrounding the Sgr B2 cloud. Figure 15a shows a low-resolution VLA continuum image of Sgr B2 at 90cm with $\text{FWHM}=41.6'' \times 22.7''$ against contoure of EW $K\alpha$ line emission. The integrated flux at 90cm is about 17 Jy which is likely to be mainly due to thermal emission from HII regions. It is difficult to disentangle nonthermal from thermal emission from this region. There is also degree-scale diffuse feature surrounding Sgr B2 based on Green Bank observations at 90cm (Law et al. 2007, in preparation). However, it is not clear how much of this large-scale diffuse emisison, which is more than sufficient to account for the origin of 6.4 keV emission, arises from Sgr B2. The total background subtracted integrated 90cm flux from the region covering Sgr A, B, C and the continuum arc is about $\sim 1200 \text{ Jy}$, most of which is expected to be nonthermal.

The large EW of Fe $K\alpha$ line emission in Sgr B2 may result from the high abundance of iron by roughly a factor of 3-4 times solar value. Other parameters that could increase the strength of EW are column density and the spectrum of the nonthermal emission, but neither of which can be important as shown in Figures 13a,b. The Galactic center molecular clouds show metallicity that is generally twice higher than in the solar neighborhood, thus we are predicting that Sgr B2 could have a 1.5-2 times higher metallicity than that of typical Galactic center clouds.

Sgr B1 lies adjacent to a number of nonthermal radio filaments with flux densities of

~ 10 mJy on the eastern side of the Sgr B1 cloud, Figure 15b shows the contour distribution of EW of $K\alpha$ emission against the grayscale 90 cm image. The prominent nonthermal filaments observed at 90 cm clearly shows their distribution with respect to the edge of $K\alpha$ line emission. The integrated 90 cm flux from the filaments shown in Figure 15b is roughly about 800 mJy. The distribution of EW over the region of Sgr B1 shown in Figure 2 ranges between few hundreds to 1500 eV near $l=34'7''$, $b=-1'13''$. The extracted spectrum over this region gives a $EW \sim 570$ eV (Table 2). Adopting a size of 77 arcmin^2 , source depth $10'$, and a $\nu^{-0.7}$ spectrum, the required electron energy density, equipartition field and resulting 90 cm synchrotron flux are 23 eV cm^{-3} , 0.030 mG and 3.2 Jy respectively.

4.4. Cosmic Ray Heating of Molecular Clouds

The heating associated with the electron energy losses is significant. It is dominated by the electrons entering the cloud with initial energies between 0.1 and 1 MeV as lower energy electrons are injected less efficiently, and higher energy electrons do not lose much of their energy in the cloud. For each erg of electron energy deposited into the cloud, approximately 10% goes into heat (Dalgarno, Yan & Liu 1999) and 200 Fe $K\alpha$ photons are produced, thus the heating rate is

$$\frac{\Gamma}{n_H} = 0.1 \times \frac{4\pi I_{K\alpha}}{N_H} \frac{2/3}{200 \text{ ph erg}^{-1}} \sim 3 \times 10^{-24} \text{ erg s}^{-1} \text{ H}^{-1} \quad (11)$$

where the factor of $2/3$ removes the contribution of $E > 10 \text{ MeV}$ electrons to $I_{K\alpha}$. This heating rate implies temperatures of $\sim 200 \text{ K}$ for $n(\text{H}_2) \sim 1 \times 10^4 \text{ cm}^3$ and $N_{\text{H}_2}/\Delta v \sim 10^{22} \text{ cm}^{-2} \text{ km}^{-1} \text{ s}$ (Neufeld, Lepp & Melnick 1995). Such a high temperature due to low energy cosmic ray heating is consistent with multi-transition ammonia line observations indicating a warm 200K gas observed throughout the Galactic center region (e.g., Hüttemeister et al. 1993b; Rodriguez-Fernandez et al. 2004; Oka et al. 2005). There is also a denser and colder component of molecular gas that has been detected to have small volume filling factor. If the denser component lies in the Galactic center, we believe that either cosmic rays have not penetrated these dense regions or that the higher cooling rate of dense gas has lowered the gas temperature.

4.5. Cosmic Ray Ionization Rate in the Galactic center

We can also estimate that the ionization of the molecular gas associated with the losses of electrons with incident energies between 0.1 and 1 MeV. The ionization rate is

readily estimated from eq (11) by noting that on average, an ionization occurs for each deposition of 40.1 eV of electron energy into the gas (Dalgarno *et al.* 1999), yielding $\zeta \approx (3 \times 10^{-24} \text{ erg s}^{-1} \text{ H}^{-1}) / (40.1 \text{ eV}) \approx 5 \times 10^{-13} \text{ s}^{-1} \text{ H}^{-1}$. This value of ζ is about 4 orders of magnitude higher than the canonical value of the interstellar cosmic-ray ionization rate and corresponds to an energetic electron energy density $\sim 1000 \text{ eV cm}^{-3}$, appropriate for Sgr C. This is reduced by 1–2 orders of magnitude for Sgr B1 and B2 and the Radio Arc (see Table 3), giving $\zeta \sim 2 \times 10^{-14} \text{ s}^{-1} \text{ H}^{-1}$ for these sources. As pointed out earlier, the detection of substantial amount of the (3,3) metastable rotational levels of H_3^+ in the Galactic center region requires an estimated high ionization rate which is estimated to be about two orders of magnitude higher than in that for diffuse clouds (Oka *et al.* 2005). Thus cosmic-rays in the Galactic center region may be responsible for producing the large reservoir of warm molecular gas which is inferred from H_3^+ measurements.

5. The Origin of Diffuse TeV Emission

Inverse Compton scattering of the sub-millimeter radiation from dust in the Galactic centre clouds by relativistic electrons may account for or significantly contribute to the diffuse TeV emission observed towards the central regions of the Galaxy (Aharonian *et al.* 2006). For example the strongest HESS peak overlays the arc (see Fig. 12). To estimate this contribution, we assume that the dust emission in the region is isotropic with intensity $I_\nu = B_\nu(T_d)(1 - \exp(-\tau_d))$ where $T_d = 20 \text{ K}$ is the dust temperature and the dust optical depth $\tau_d \propto \nu^2$ (Pierce-Price *et al.* 2000). The $850\mu\text{m}$ and $400\mu\text{m}$ SCUBA maps yields an estimate of $\tau_d = 0.029$ at $\nu = kT_d/h$. The electron spectrum associated with the arc must extend to at least 30 TeV to produce upscattered photons at TeV energies. An extrapolation of the E^{-2} electron spectrum that obtains at GeV energies into the TeV range predicts a photon flux at 1 TeV that is sixty times that observed, which we estimate to be $\sim 1 \times 10^{-13} \text{ ph cm}^{-2} \text{ s}^{-1}$ (Aharonian *et al.* 2006). However one expects a synchrotron break at lower energies, and the observed TeV spectrum has a photon index of ~ -2.3 , steeper than the -1.5 this simple model would predict. Instead we assume that synchrotron losses steepen the electron spectrum at energies above 2 TeV to an E^{-3} dependence; the corresponding synchrotron loss time scale is 1000 years. This steepens the predicted ICS photon spectrum from $E_\gamma^{-1.5}$ to E_γ^{-2} above 40 GeV and matches the observed HESS flux at 1 TeV.

6. Conclusions

The distributions of ^{13}CO line, X-ray, nonthermal radio continuum and 6.4 keV line emission suggest against the irradiation origin of X-ray emission from Sgr C. We believe that the origin of X-ray continuum and line emission can naturally be explained by the interaction of cosmic rays with prominent Galactic center molecular clouds such as Sgr C, the “45 and -30 km s^{-1} clouds”, Sgr B1 and Sgr B2. We have argued that the sources of nonthermal particles are due to a combination of the Galactic center radio filaments which are localized in the immediate vicinity of molecular clouds, as well as the diffuse nonthermal component distributed throughout the Galactic center region. This hypothesis is consistent with similar value of 6.4 keV equivalent width throughout the Sgr C, the -30 & 45 km s^{-1} clouds near the radio arc and Sgr B1 regions.

In the context of this model, we explain the high value of the equivalent width of Fe $K\alpha$ line and unusually strong $K\alpha$ line emission from Sgr B2 in terms of higher metallicity and the contribution of a diffuse nonthermal particles in this source. The interaction of the nonthermal radio filaments and the molecular cloud implies that these features are at the same distance from each other and that the long-standing problem of the origin of high temperature molecular gas can naturally be explained in terms of the LECR heating of the clouds. In addition, we estimate the high cosmic-ray ionization rate in the Galactic center region which could explain the origin of warm molecular gas as traced by H_3^+ absorption study. In addition, we provide an alternative model to explain the origin of diffuse TeV emission from molecular clouds in the central region of the Galaxy by using the high energy component of nonthermal electrons to upscatter the submillimeter emission from dust clouds in this region. The remarkable correlation of $K\alpha$ line emission, TeV emission and molecular gas suggest that similar processes are at work in explaining both diffuse X-ray and γ -ray emission from the Galactic center clouds. Lastly, we believe that the interplay between the cosmic rays and neutral gas in the central region of the Galaxy is significant and provides much insight in our understanding of the physical processes that are involved in both the nuclei and the disk of galaxies.

Acknowledgments: We are grateful to J. Hinton, N. Kassim, D. Pierce-Price & Y. Tsuboi for providing us with their published data. D. Lis is supported by NSF grant AST-0540882 to Caltech Submillimeter Observatory.

7. Appendix

7.0.1. Polarization Measurements

Additional support for the synchrotron nature of the filament comes from polarization measurements. We carried out high frequency polarization study of Sgr C at 3.6 cm to reduce the effect of Faraday rotation toward this source. Figure 10a shows a grayscale image of linearly polarized emission from the linear filament of Sgr C with line segments indicating the polarization angle distribution at 3.6 cm. The peak emission has a flux density of 1.4 mJy beam^{−1} near the center of the image and ~ 0.28 mJy beam^{−1} away from the center. The degree of polarization is remarkably high corresponding to a value of about 65%. In contrast, the region to the south of this highly polarized feature, the polarization degree drops off to 10% near the compact source G359.45–0.05. The low degree of linear polarization to the south of the filament could be due to the contamination by the bright thermal emission from Sgr C H II region. This diffuse H II region is likely responsible for depolarization of synchrotron emission from the Sgr C filaments. Due to high Faraday rotation toward the Galactic center sources, we are not able to determine the intrinsic direction of the magnetic field along the Sgr C filament. Assuming that depolarization is caused by an external medium, the lack of strong polarized emission to the south suggests that the filament lies either behind the H II region or is embedded within it.

Figure 10b shows a grayscale image of Sgr C at 3.6 cm with a resolution $9.8'' \times 7.5''$ (PA= -7.5°). We note several circular-like extended features to the north and south of the Sgr C filament, as well as a bright compact source along the filament. These features generally show a flatter spectrum than the linear filament. The compact source G359.45–0.05 ($l=359^\circ 27' 19.94'' \pm 0.002$, $b=-03' 22.49'' \pm 0.04$) has a spectral index of $\sim -0.29 \pm 0.21$ between 3.6 and 2 cm. Other extended sources identified as G359.45–0.07, G359.45–0.03 and G359.45–0.02 in Figure 9, all of which appear to be thermal sources having mean spectral index values $\alpha = -0.1 \pm 0.24$, -0.09 ± 0.3 and -0.02 ± 0.3 , respectively. It is difficult to determine the true relationship between these features and the nonthermal filament with the available resolution. In particular, the ring-shaped morphology of G359.45–0.07, in which the nonthermal filament appears to pass through the ring, as well as the compact source G359.45–0.5. We also note a weak vertical filament to the south of the Sgr C H II region directed south of galactic latitude $b=-6'$, as shown in Figure 10b. This feature needs to be confirmed as it falls outside the primary beam of our 3.6 cm image and that it has never been detected in previous radio continuum images of Sgr C.

REFERENCES

- Anantharamaiah, K. R., Pedlar, A., Ekers, R. D. & Goss, W. M. 1991, MNRAS, 249, 262
- Aharonian, F. et al. 2006, Nature, 439, 695
- Arnaud, K.A., 1996, Astronomical Data Analysis Software and Systems V, eds. Jacoby G. and Barnes J., p17, ASP Conf. Series volume 101
- Anantharamaiah, K.R. & Yusef-Zadeh, F. 1989, in the center of the Galaxy, IAU Symp. 136. ed. M. Morris (Kluwer Academic Publisher, Dordrecht), p159
- Armstrong, J.T. & Barrett, A.H. 1985, ApJ, 57, 535
- Belanger, G., Goldwurm, A., Renaud, M., Terrier, R., Melia, F., Lund, N., Paul, J., Skinner, G. & Yusef-Zadeh, F. 2006, ApJ, 636, 275
- Boldyrev, S. & Yusef-Zadeh, F. 2006, ApJ, 637, L101
- Caswell, J.L. & Haynes, R.F. 1987, A&A, 171, 261
- Coil, A. & Ho, P.T.P. 2000, ApJ, 533, 245
- Cotera, A., Erickson, E., Colgan, S., Simpson, J., Allen, D. & Burton, M. 1996, ApJ, 461, 750
- Dalgarno, A., Yan, M. & Liu, W. H. 1999, ApJSupp, 125, 237
- ownes, D., Goss, W. M., Schwarz, U. J. & Wouterloot, J. G. A. 1979, A&AS, 35, 1
- kers, R. D., van Gorkom, J. H., Schwarz, U. J. & Goss, W. M. 1983, A&A, 122, 143
- Erickson, N.R., Goldsmith, P.F., Novak, G., Grosslein, R.M., Viscuso, P.J., Erickson, R.B., & Predmore, C.R. 1992, IEEE Trans, Microwave Theory Tech. 40, 1
- Figer, D.F., Sungsoo, S.K., Morris, M., Serabyn, E., Rich, R.M., McLean, I.S. 1999, ApJ, 525, 750
- Frerking, M. A., Langer, W. D. & Wilson, R. W. 1982, ApJ, 262, 59
- Fryer, C. L., Rockefeller, G., Hungerford, A. & Melia, F. 2006, ApJ, 638, 786
- Giveon, U., Morisset, C. & Sternberg, A. 2002, A&A 392, 501
- Gray, A.D. 1994, MNRAS, 270, 861

- Güsten, R., Walmsley, C.M. & Pauls, T. 1981, A&A, 103, 197
- Handa, T., Sakano, M., Naito, S. & Hiramatsu, M. 2006, ApJ, 636, 261
- elfand, D. J. & Becker, R. H. 1987, ApJ, 314, 203
- Ho, P.T.P., Jackson, J.M., Barrett, A.H. & Armstrong, J.T., 1985, ApJ, 288, 575
- Hüttemeister, S., Wilson, T.L., Banina, T.M., Martin-Pintado, J. 1993b, A&A, 280, 255
- Hüttemeister, S., Wilson, T., Henkel, C. & Mauserberger, R. 1993a, A&A, 276, 445
- ICRU 1984, International Commission on Radiation Units and Measurements Report 37
- assim, N. E. & Frail, D. A. 1996, MNRAS, 283, L51
- Koyama, K., Maeda, Y., Sonobe, T., Takeshima, T., Tanaka, Y. *et al.* 1996, PASJ, 48, 249
- Lang, C.C., Goss, W.M. & Morris, M. 2002, AJ, 124, 2677
- Lang, C., Morris, M. & Echevarria, L. 1999, ApJ, 526, 727
- Law, C. 2006, PhD thesis, Northwestern University
- Law, C. & Yusef-Zadeh 2004, ApJ, 611, 858
- Lis, D. C.& Carlstrom, J. E. 1994, ApJ, 424, 189
- Lis, D.C., & Goldsmith, P.F. 1989, ApJ 337, 704
- Lis, D.C., & Goldsmith, P.F. 1991, ApJ 369, 157
- Liszt, H.S. 1992, ApJS, 82, 495
- Liszt, H.S., & Spiker, R.W. 1995, ApJS, 98, 259
- Lu, F.G., Wang, Q.D. & Lang, C.C. 2003, AJ, 126, 319
- Mehring, D.M., Yusef-Zadeh, F., Palmer, P., & Goss, W.M. 1992, ApJ, 401, 168
- Murakami, H., Koyama, K., Tsujimoto, M. & Maeda, Y. 2001a, ApJ, 550, 297
- Murakami, H., Koyama, K. & Maeda, Y. 2001b, ApJ, 558, 687
- Murakami, H., Koyama, K., Sakano, M., Tsujimoto, M., Maeda, Y. 2000, ApJ, 534, 284
- Muno, M. P., Bauer, F.E., Bandyopadhyay, R.M. & Wang, Q.D. 2006, ApJS, 165, 173

- Muno, M. P. *et al.* 2004a, ApJ, 613, 326
- Muno, M. P. *et al.* 2004b, ApJ, 613, 1179
- Neufeld, D. A., Lepp, S. & Melnick, G. J. 1995, ApJ Supp, 100, 132
- Nord, M.E., Lazio, T.J.W., Kassim, N.E., Hyman, S.J., LaRosa, T.N., Brogan, C.L. & Duric, N., 2004, AJ, 128, 1646
- Odenwald, S. F. & Fazio, G. G. 1984, ApJ, 283, 601
- Oka, T., Geballe, T.R., Gotto, M., Usida, T. & McCall, B. 2005, ApJ, 632, 882
- Oka, T., Hasegawa, T., Sato, F., Tsuboi, M. & Miyazaki, A. 2001, PASJ, 53, 779
- Park, S., Baganoff, F. K., Morris, M., Maeda, Y., Muno, M. P., Howard, C., Bautz, M. W., & Garmire, G. P. 2004, ApJ, 603, 548
- Pierce-Price, D., Richer, J. S., Greaves, J. S., Holland, W. S., Jenness, T., Lasenby, A. N. et al. 2000, ApJ, 545, 121
- Reich, W. 2003, A&A, 401, 1023
- Revnivtsev, M. G., Churazov, E. M., Sazonov, S. Yu., Sunyaev, R.A., Lutovinov, A. A. et al. 2004, A&A, 425, 49
- Rodriguez-Fernandez, N.J., Martin-Pintado, J., Fuente, A., de Vicente, P., Wilson, T.L. & Hüttemeister 2001, A&A, 365, 174
- Rodriguez-Fernandez, N.J., Martin-Pintado, J., Fuente, A. & Wilson, T.L. 2004, A&A, 427, 217
- Roy, S. 2003, A&A, 403, 917
- Rudolph, A. L., Fich, M., Bell, G. R., Norsen, T., Simpson, J., P., Haas, M. R. & Erickson, E. F 2006, ApJS, 162, 346
- Sakano, M., Warwick, R.S., Decourchelle, A. & Predhel, P. 2003, MNRAS, 340, 747
- Serabyn, E. & Güsten, R. 1987, A&A, 184, 133
- Sunyaev, R.A., Markevitch M. & Pavlinsky, M. 1993, ApJ, 407, 606
- Tatischeff, V. 2003, in Final stages of stellar evolution, ed. C. Motch & J.-M. Hameury, EAS Pub Ser, 79

- Townsley, L. K. *et al.* , 2002b, NIM-A, 486, 751
- Tsuboi, M., Kobayashi, H., Ishiguro, M. & Murata, Y. 1991, PASJ, 43, L27
- Tsuboi, M., M., Ukita, N., & Handa, T. 1997, ApJ, 481, 263
- Valinia, A. & Marshall, F.E. 2000, ApJ, 505, 134
- van der Tak, F.F.S., Belloche, A., Schilke, P., Güsten, R., Philipp, S., Comito, et al. 2006, A&A, in press
- Wang, Q.D., Dong, Hui & Lang, C. 2006, ApJ (in press)
- Wang, Q. D., Gotthelf, E. V., & Lang, C. C. 2002, Nature, 415, 148
- Weisskopf, M. C., Brinkman, B., Canizares, C., Garmire, G., Murray, S., & van Speybroeck, L. P. 2002, PASP, 114, 1
- Wilson, T.L. & Rood, R. 1994, ARAA 32, 19
- Yusef-Zadeh, F., 2003, ApJ, 598, 325
- Yusef-Zadeh, F. 1986, PhD thesis, Columbia University
- Yusef-Zadeh, F., Hewitt, J. W., & Cotton, W. 2004, ApJS, 155, 421
- Yusef-Zadeh, F., Law, C. & Wardle 2002, ApJ, 568, L121
- Yusef-Zadeh, F., Morris, M., & Chance, D., 1984, Nature, 310, 557
- Yusef-Zadeh, F., Morris, M., Slee, O.B. & Nelson, G.J. 1986, ApJ, 310, 689
- Yusef-Zadeh, F., Nord, M., Wardle, M., Law, C., Lang, C. & Lazio, T.J.W. 2003, ApJ, 590, L103
- Yusef-Zadeh, F.; Wardle, M.; Munro, M.; Law, C.; Pound, M. 2005, AdSR, 35, 1974

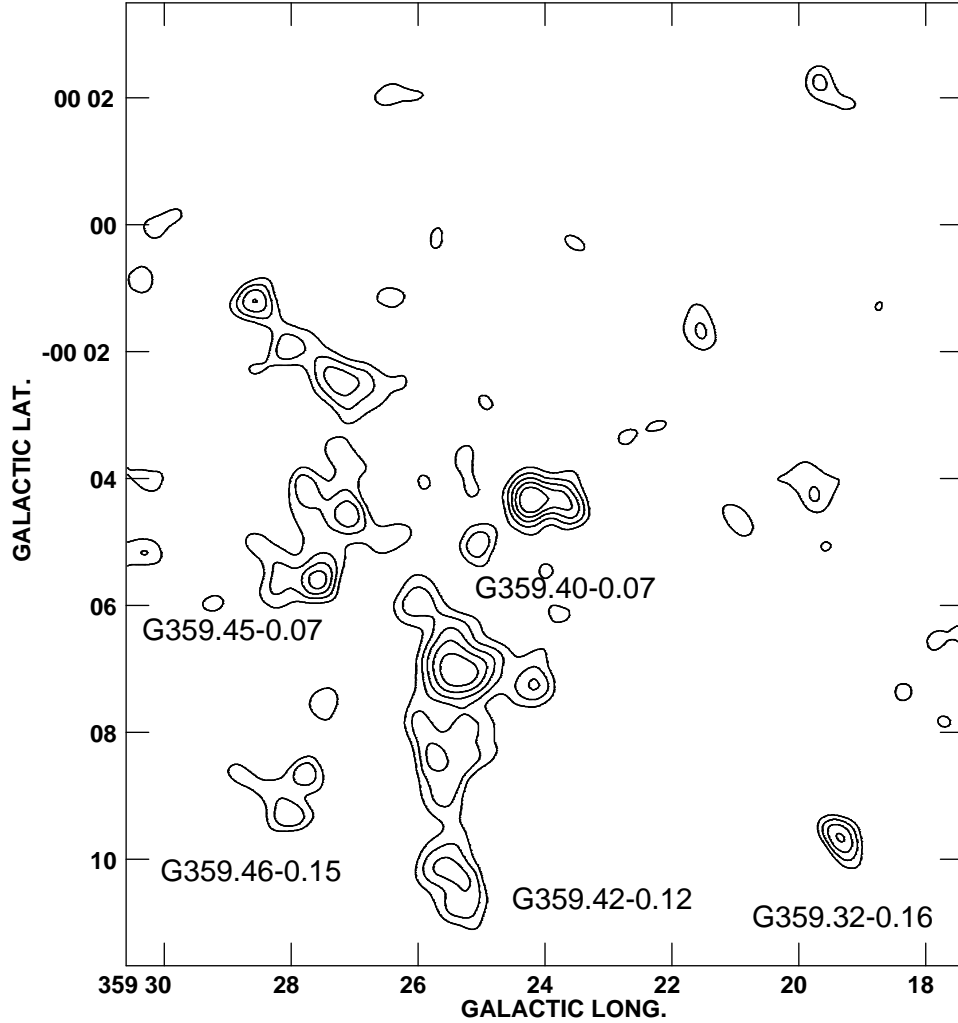


Fig. 1.— **(a)** Contours of X-ray continuum emission between 2 and 6 keV. The X-ray data are convolved with a Gaussian beam having $\text{FWHM} \sim 30''$. Contour levels are set at $(7, 8, 9, 10, 11) \times 10^{-9}$ Jy per beam. The diffuse and compact X-ray continuum features are labeled. **(b)** The top and bottom panels show modeling of the X-ray spectrum of diffuse emission from Sgr C and the corresponding residuals in the bottom panel. The thick solid line is the model, the dashed and the thin solid lines correspond to the 5 and 1 keV plasma components, the dot-dashed line is the emission line from low-ionization iron, and the dot-dot-dot-dashed line is the power law. The residuals are in units of the 1-sigma uncertainty on the spectrum. As shown in Figure 2, the spectrum was taken from an ellipse centered on $l=359.43382^\circ$, $b=-0.09655^\circ$ with a radii of $4.1'$ and $2.9'$ along the l and b directions, respectively ($\text{PA}=28.6^\circ$).

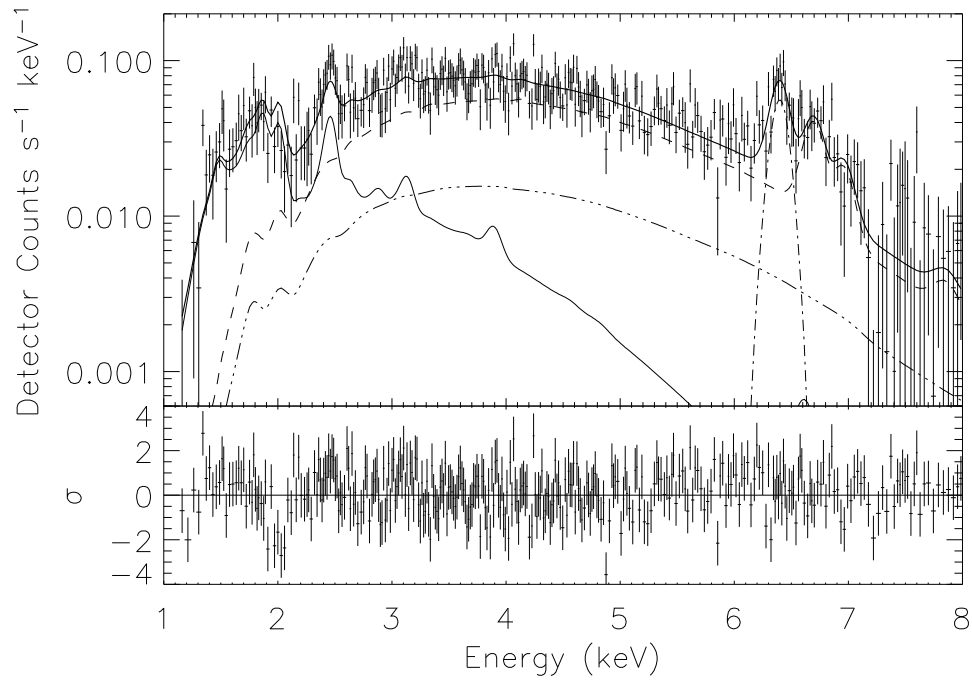


Fig. 1b. —

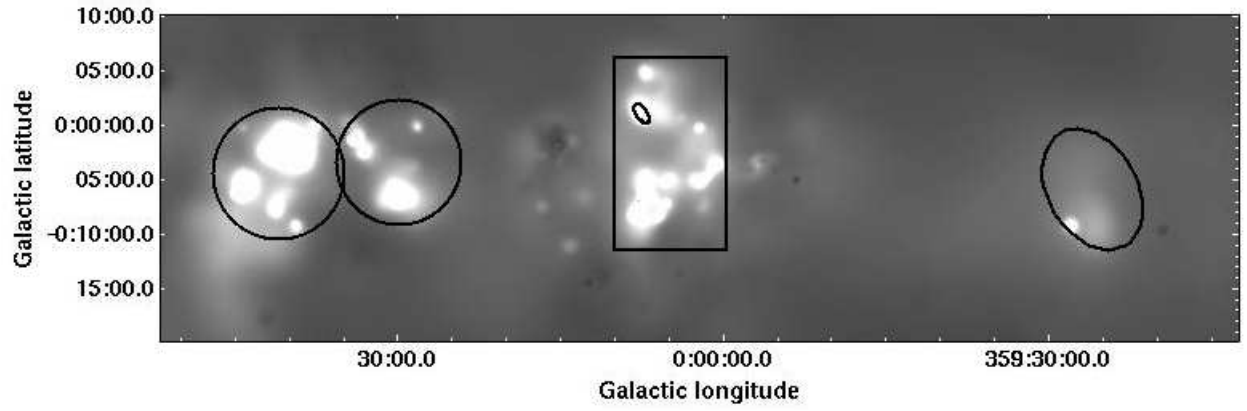


Fig. 2.— A distribution of $K\alpha$ 6.4 keV EW line emission. The regions from which X-ray spectra are extracted are drawn as an ellipse (Sgr C, the Arches cluster), a rectangle (the arc) and circles (Sgr B1 and Sgr B2).

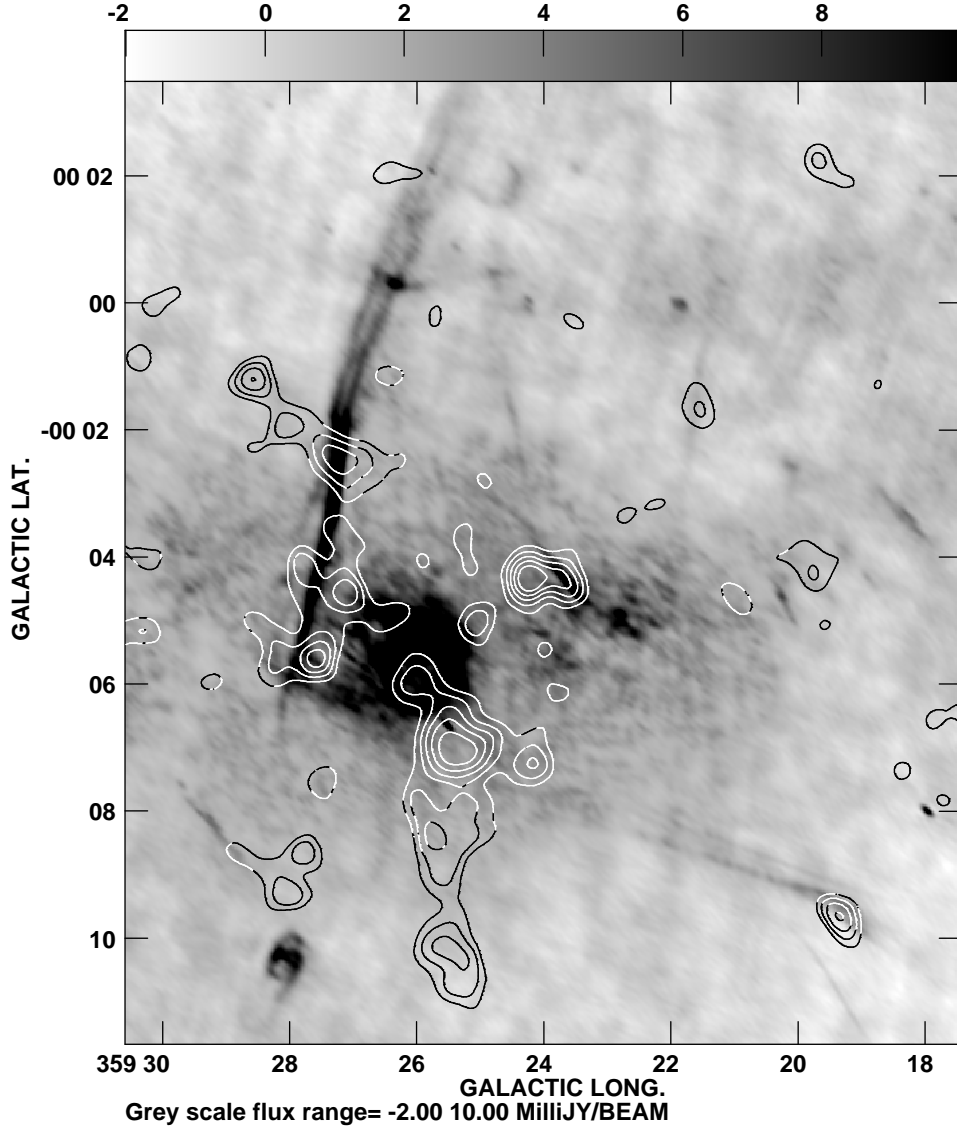


Fig. 3.— **(a)** Contours of X-ray emission between 2 and 6 keV are superimposed on a 20 cm continuum image with a resolution of $9.8'' \times 4.2''$ (PA= -12°). The contour levels are set at $(7, 8, 9, 10, 11) \times 10^{-9}$ Jy. The X-ray data are convolved by a Gaussian having FWHM= $30''$. **(b)** Contours of X-ray emission are the same as in (a). The surface brightness of a 20 cm continuum image with a resolution of $30''$ ranges between -9 and 200 mJy beam $^{-1}$ in order to bring out the faint features. **(c)** Contours of X-ray emission are the same as in (a). The surface brightness of a 90 cm continuum image with a resolution of $12.6'' \times 6.8''$ (PA= 3°) taken from Nord et al. (2004). **(d)** A close-up view of G359.32-0.1 with contours of X-ray emission superimposed on a 20 cm continuum image (in grayscale) with a spatial resolution of $8.1'' \times 3.3''$ (PA= -11°). The contour levels are set at 0.8, 1, 1.2, 1.4 nJy. The X-ray image is convolved to a $9''$ Gaussian.

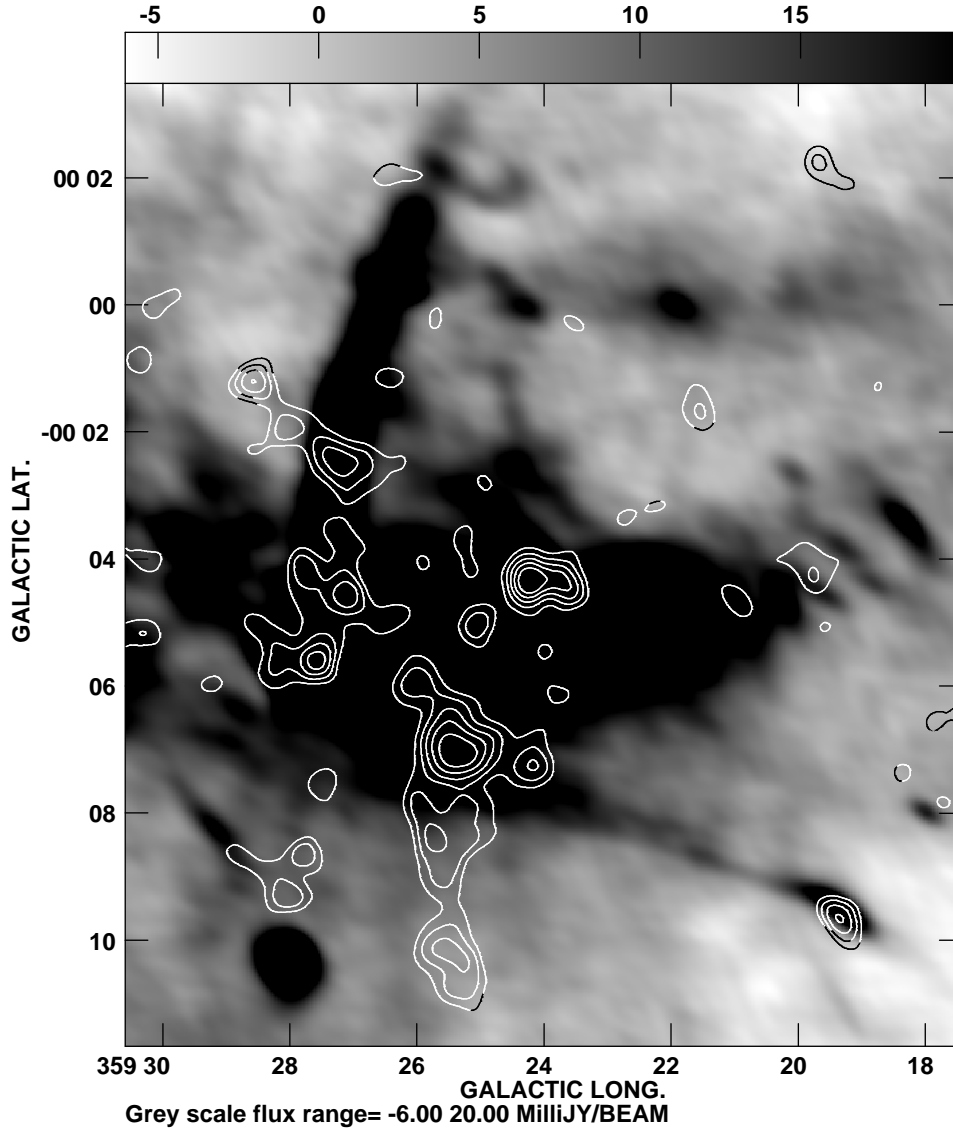


Fig. 3b. —

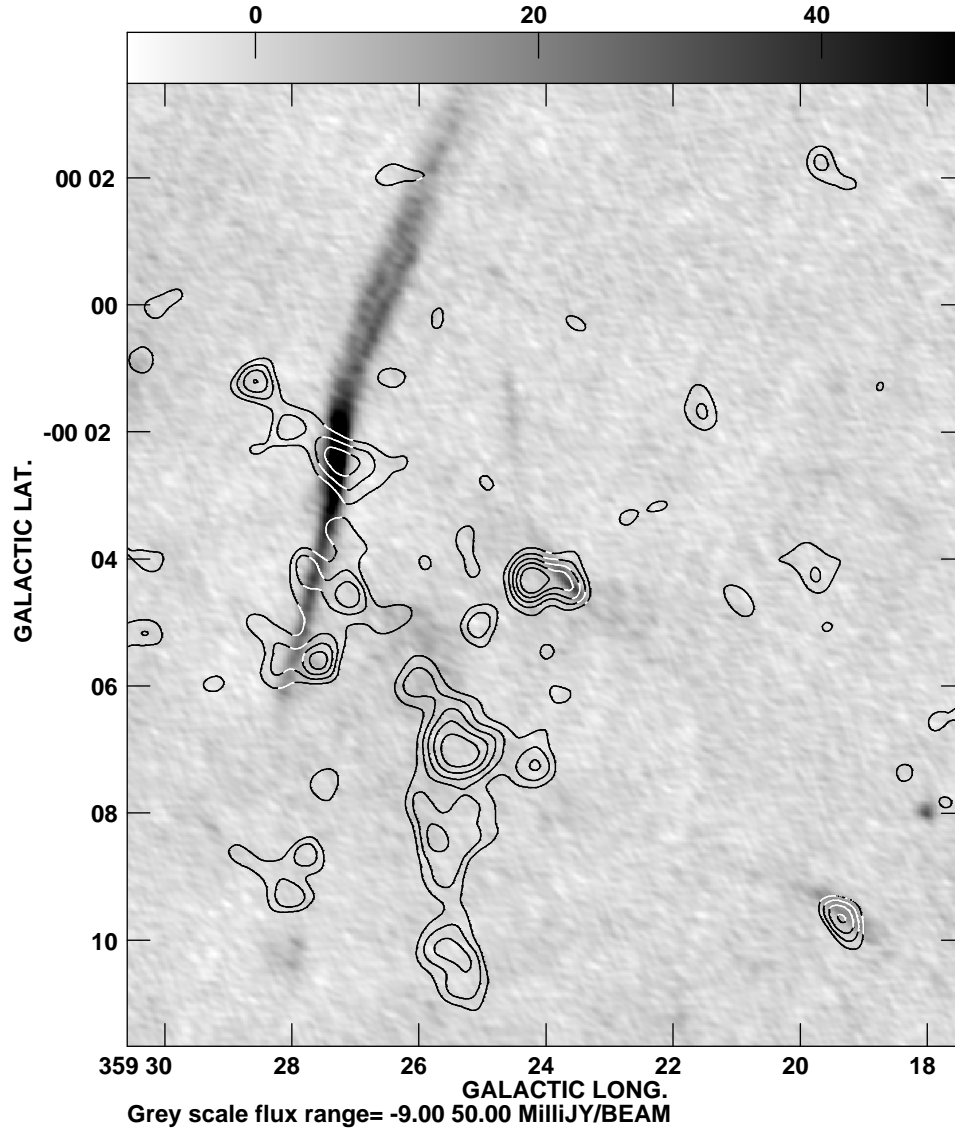


Fig. 3c. —

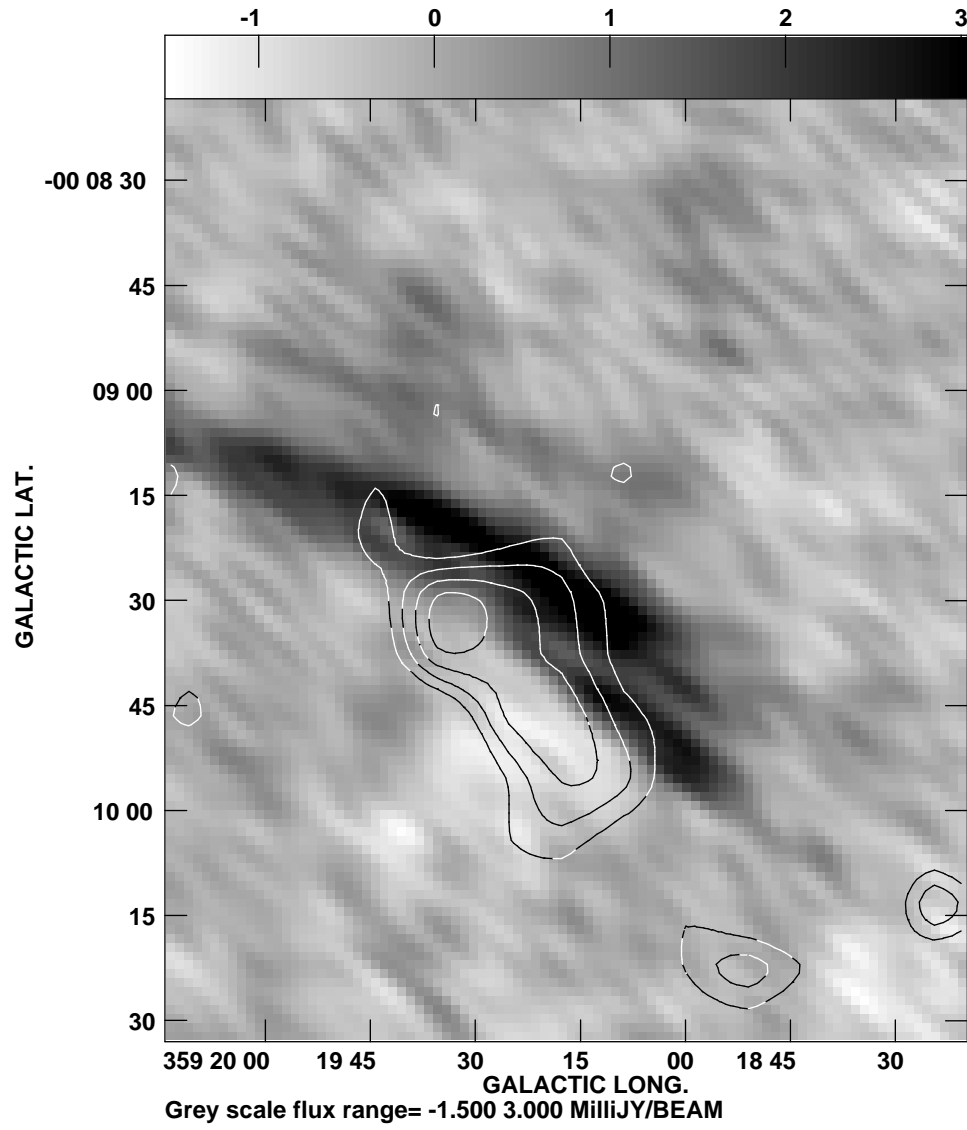


Fig. 3d. —

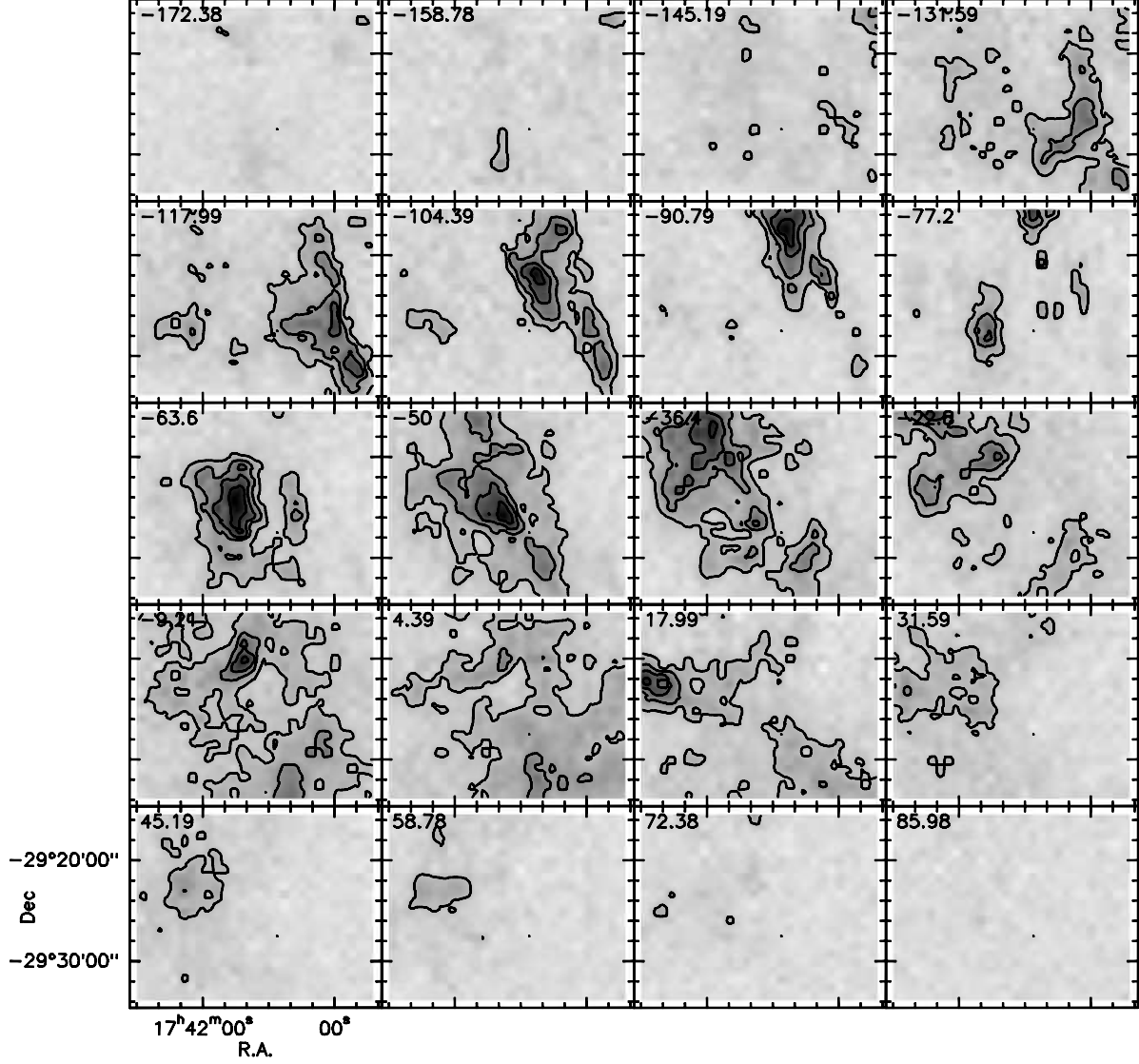


Fig. 4.— ^{13}CO (1–0) velocity channel maps. Channel center velocities are given in the upper-left center of each panel. The emission associated with the Sgr C cloud is seen in the central part of the map in the -77 to -36 km s^{-1} panels. Contour levels are -0.5 , 0.5 , 1 , 1.5 , and 2 K. The emission has been corrected for the atmospheric attenuation and warm losses, but not for the main beam efficiency ($\eta = 0.4$). This figure is shown in J2000 celestial coordinates.

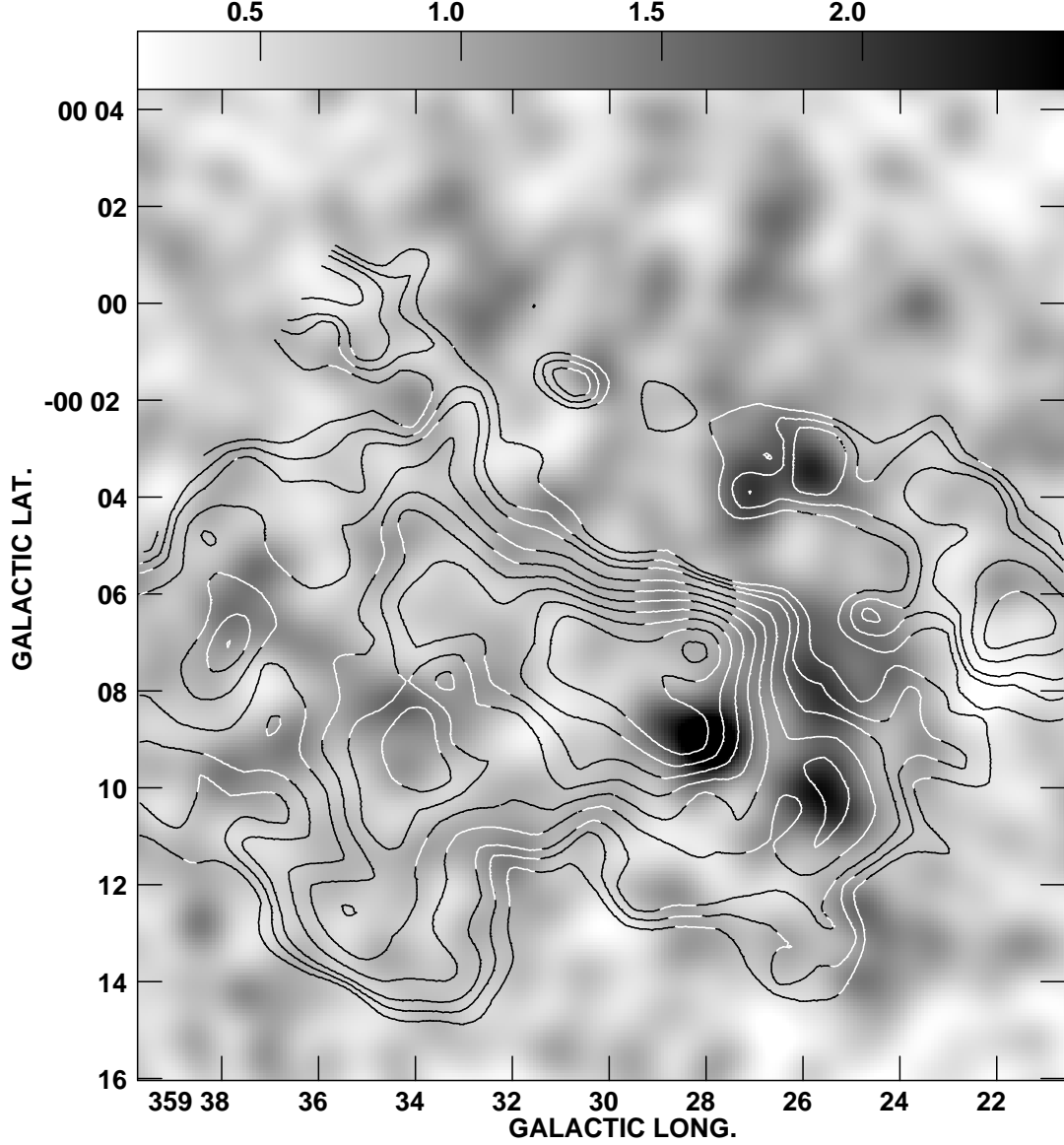


Fig. 5.— **(a)** Contours of velocity integrated ^{13}CO emission between -77.2 and -22 km s^{-1} are superimposed on a grayscale $6.4 \text{ keV K}\alpha$ line emission in grayscale with a $30''$ resolution. Contour levels are set at $(2, 2.25, 3, 3.5, 4, 4.5, 5, 5.5, 6) \times 14 \text{ K km s}^{-1}$. **(b)** Similar to **(a)** except that the grayscale (grayscale) shows the continuum X-ray emission with $60''$ spatial resolution between 2 and 6 keV. **(c)** Contours of X-ray continuum emission are superimposed on a grayscale equivalent width map of 6.4 keV line emission.

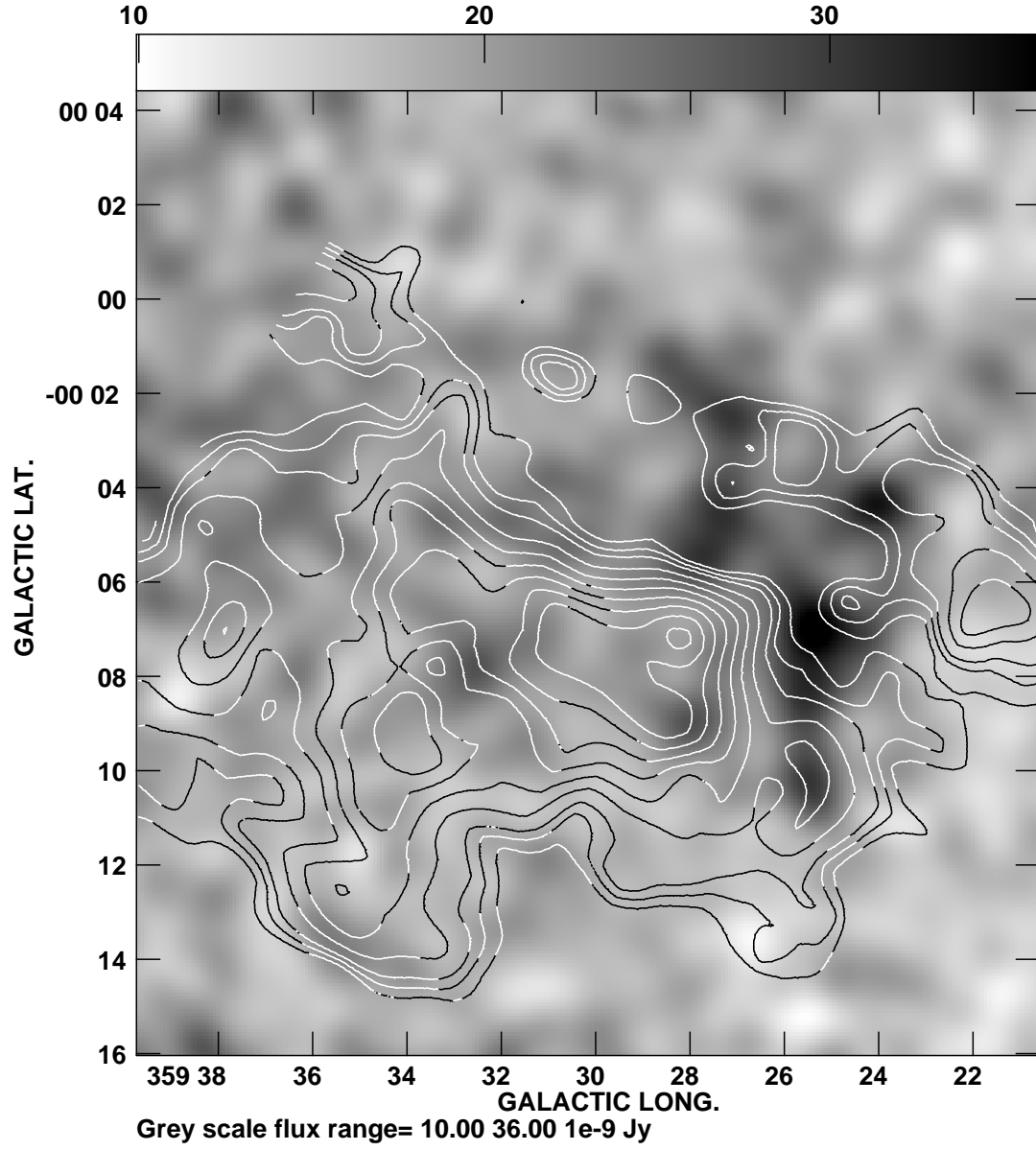


Fig. 5b. —

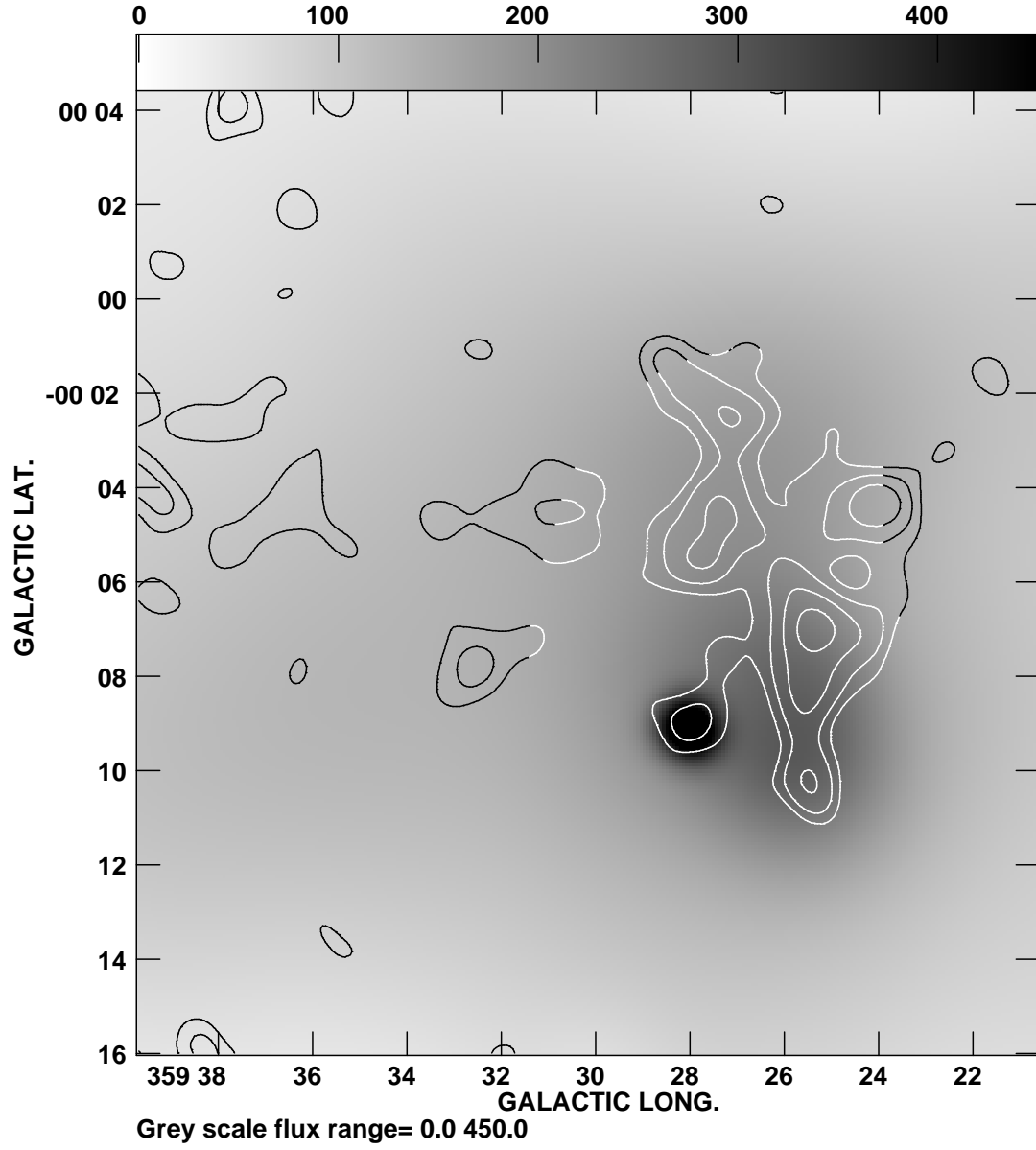


Fig. 5c. —

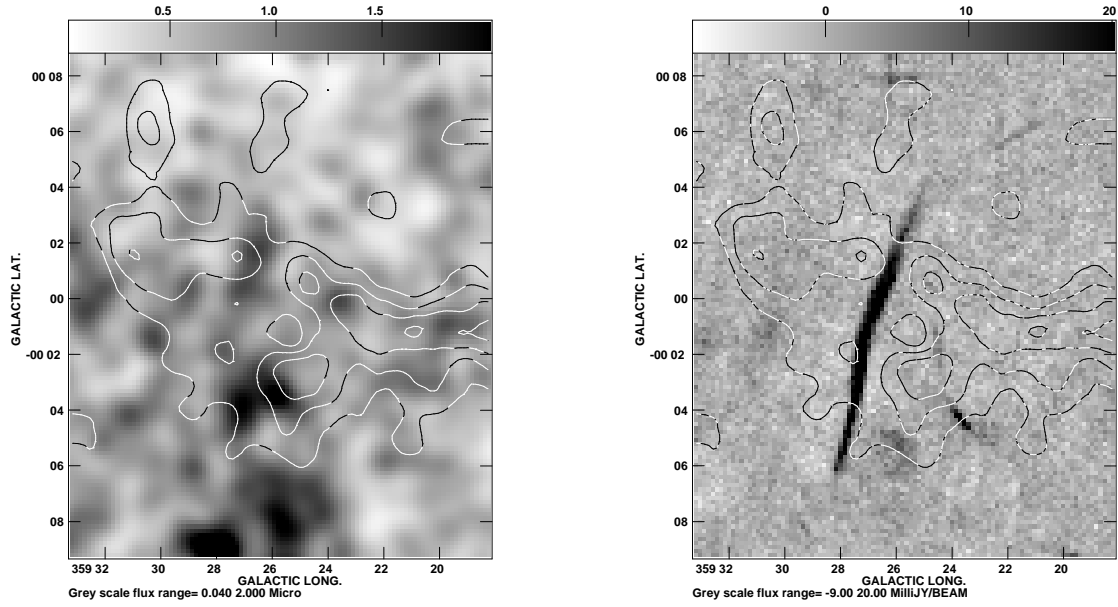


Fig. 6.— **(a)** A plot of the spectral index distribution along the brightest nonthermal vertical filament of Sgr C. **(b)** Similar to (a) except that the slice plot shows 1σ error bars of the spectral index distribution. These measurements are based on the 20 and 90 cm images convolved to a Gaussian beam having $\text{FWHM}=12.6''^2$.

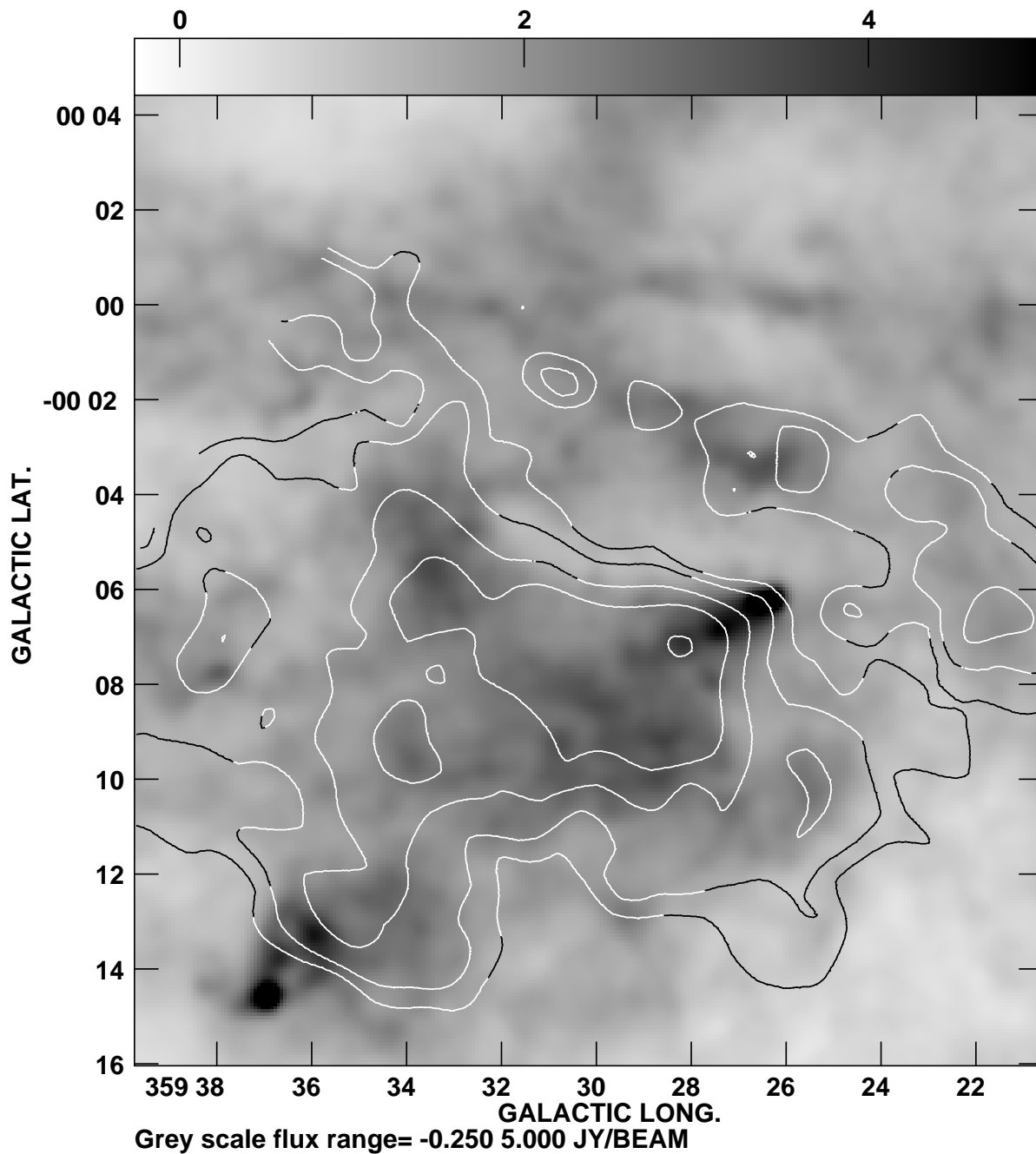


Fig. 7.— Contours of ^{13}CO molecular line emission are superimposed on a grayscale submillimeter image at $850\mu\text{m}$ taken from Pierce-Price et al. (2000) convolved to a resolution of $15''$.

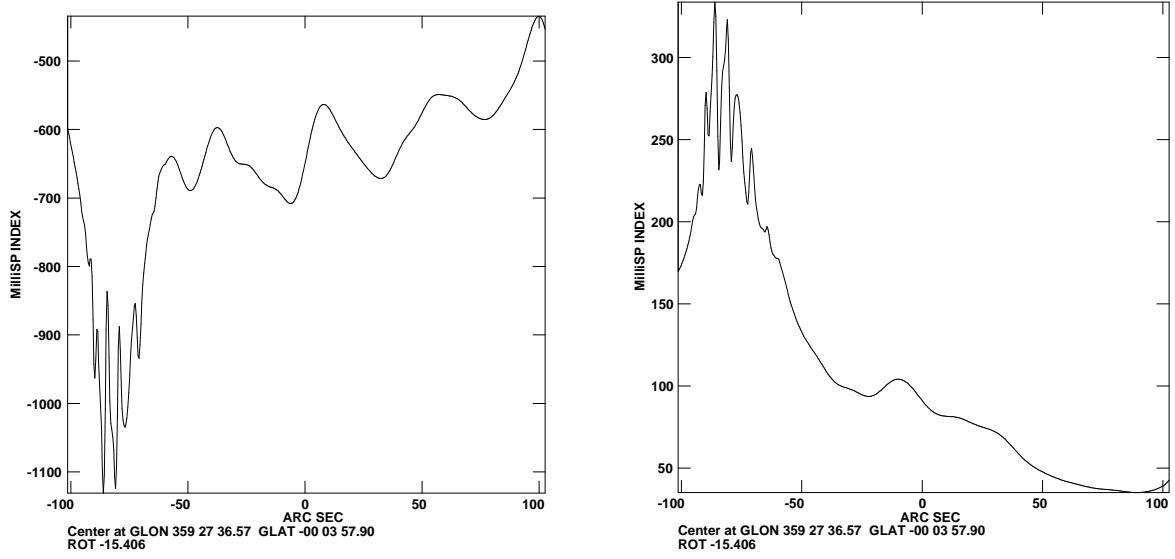


Fig. 8.— **(a)** A plot of the spectral index distribution along the brightest nonthermal vertical filament of Sgr C. **(b)** Similar to (a) except that the slice plot shows 1σ error bars of the spectral index distribution. These measurements are based on the 20 and 90 cm images convolved to a Gaussian beam having $\text{FWHM}=12.6''^2$.

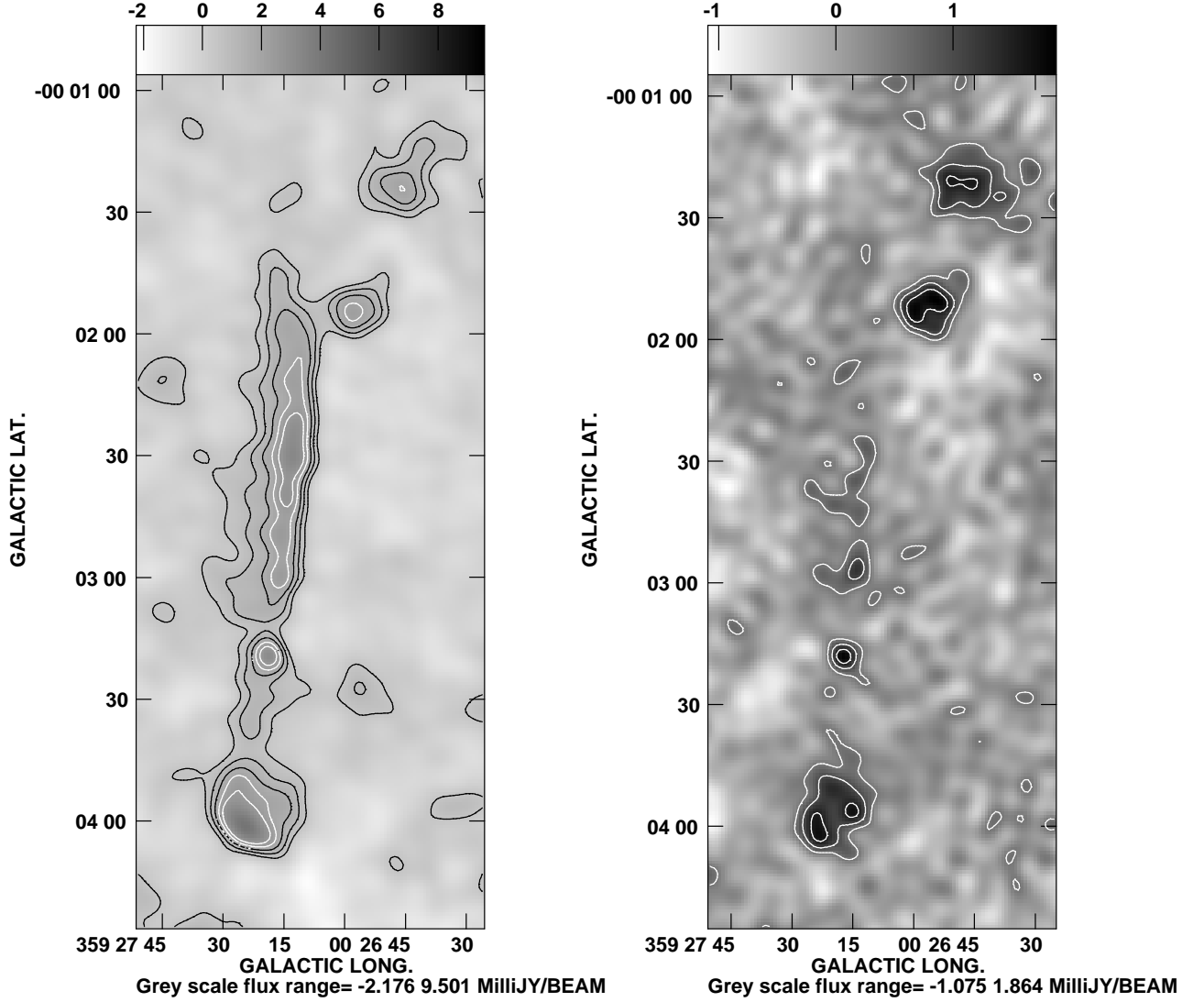


Fig. 9.— **(a) Left** A grayscale continuum image of the bright filament of Sgr C at 3.6 cm with contours set at $0.25 \times (2, 4, 6, 8, 10)$ Jy beam $^{-1}$. The rms noise is 0.24 mJy and the spatial resolution is $6.8'' \times 6.4''$ (PA=10.2°). **(b) Right** Identical to (a) except that 2 cm contours are set at $0.25 \times (2, 4, 6)$ Jy beam $^{-1}$. Both images are constructed by using the same uv range (2 – 30 k λ) to insure the same spatial frequency coverage.

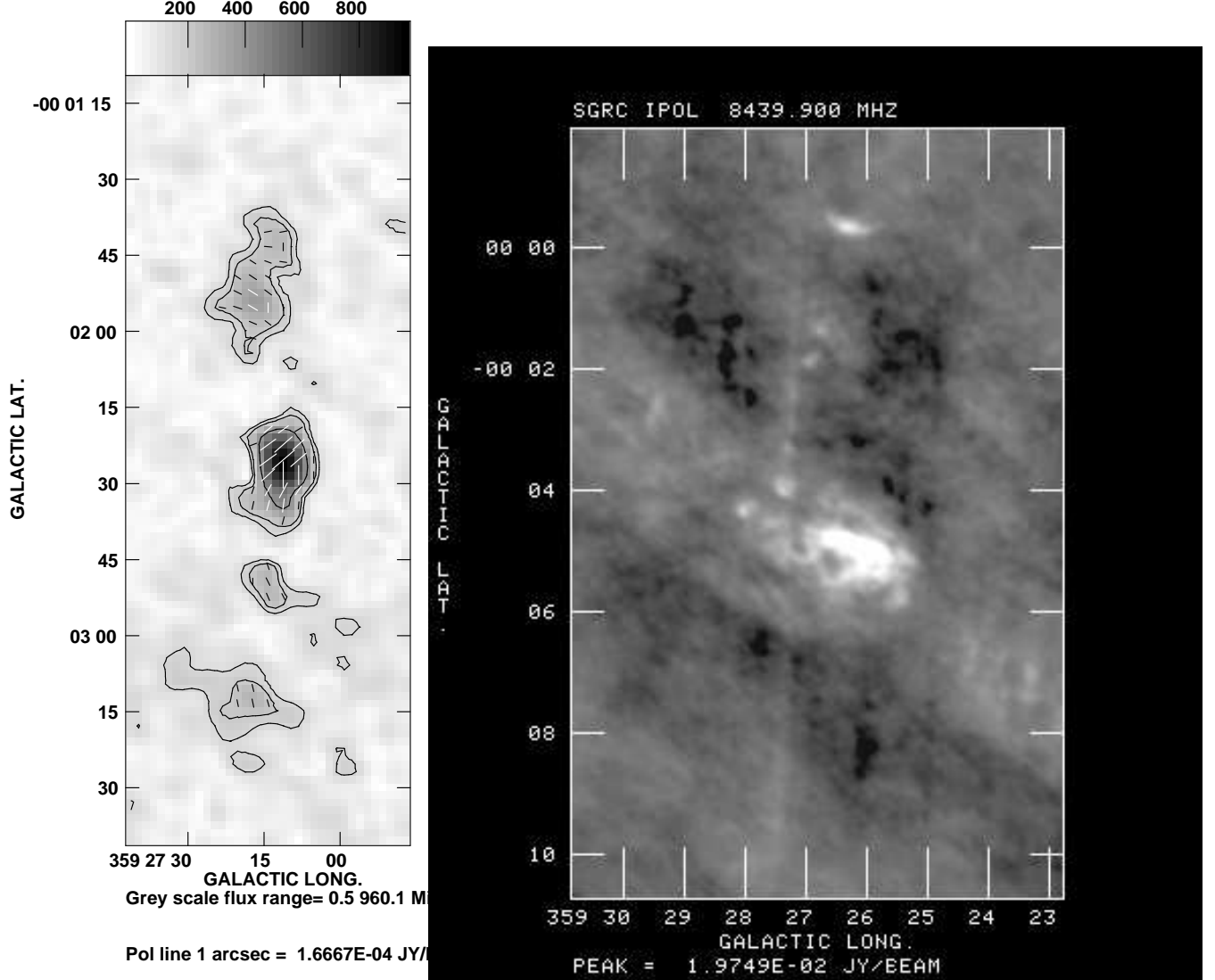


Fig. 10.— **(a) Left** A grayscale linearly polarized continuum emission from the bright filament of Sgr C at 3.6 cm with contours set at 0.15, 0.2, 0.4 mJy beam⁻¹ and the resolution of 7.9'' × 6.7'' (PA=−6.6°). The length of the line segments presents the strength of the polarized emission (1'' corresponds to 0.166 mJy beam⁻¹) whereas the position angle of the line segments shows the polarization angle distribution. **(b) Right** A grayscale image of Sgr C at 3.6 cm with a resolution of 9.8'' × 7.5'' (PA=−7.5°). This image is not corrected for the response of the primary beam. The weak filament to the south lies outside the FWHM of the primary beam.

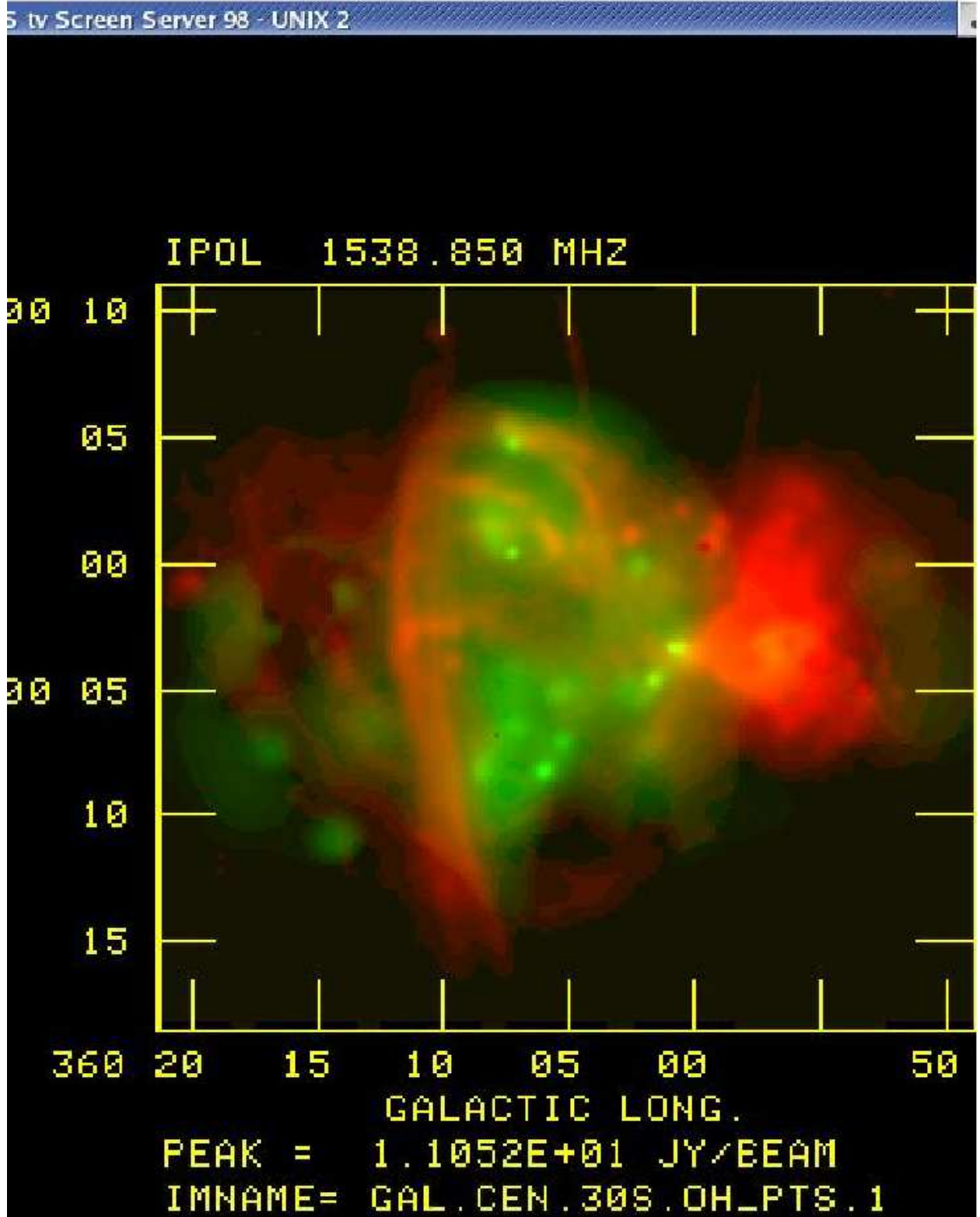


Fig. 11.— (a) A 20 cm continuum image of the Sgr A complex and the radio arc in Galactic coordinates (red color) is shown against the distribution of the 6.4 keV K α line emission (green color). (b) A 20 cm continuum image of the Sgr A complex and the radio arc in Galactic and celestial coordinates against contours of ammonia line emission from prominent molecular clouds in the Galactic center region (Güsten et al. 1981; Yusef-Zadeh 1986). (c)

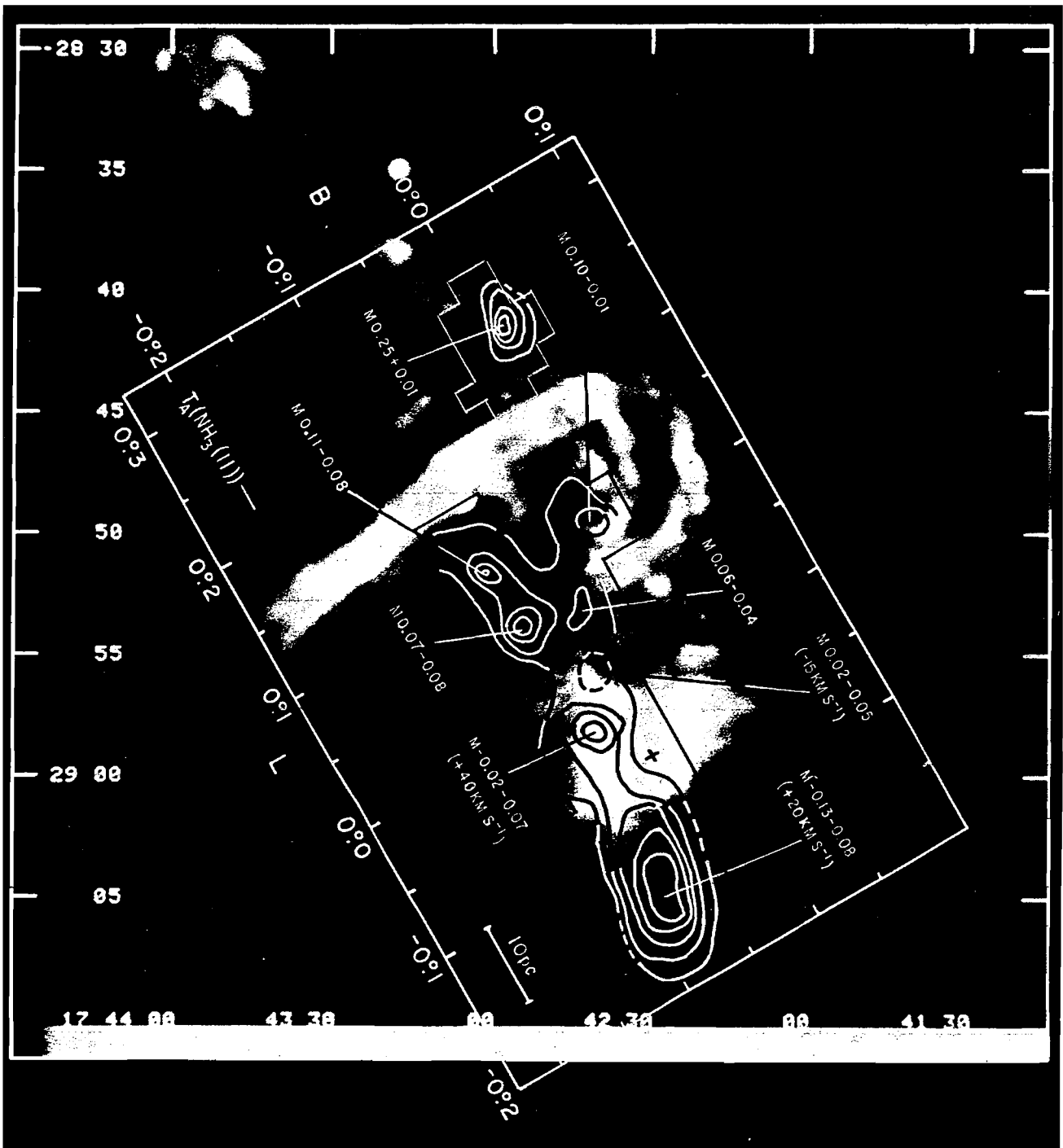


Fig. 10b. —

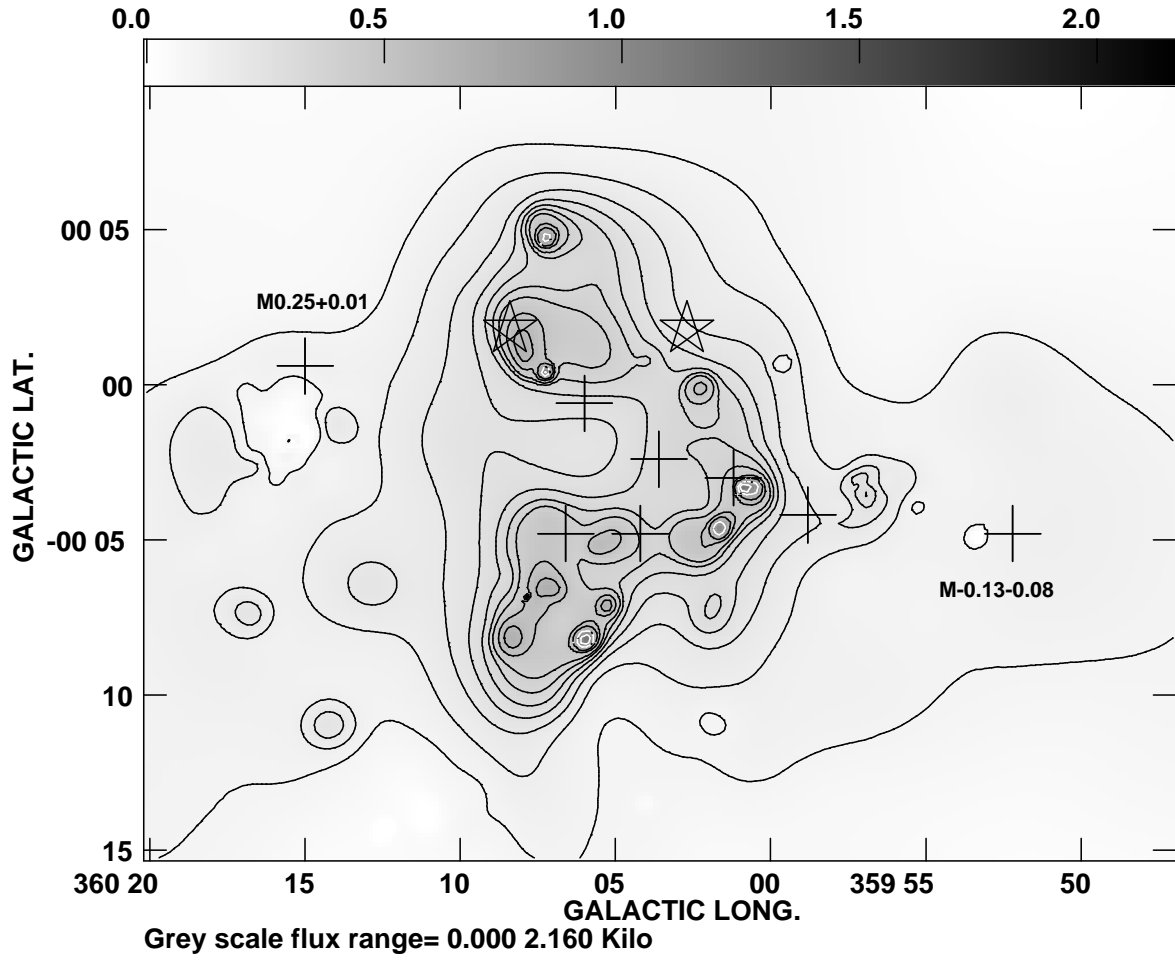


Fig. 11c. —

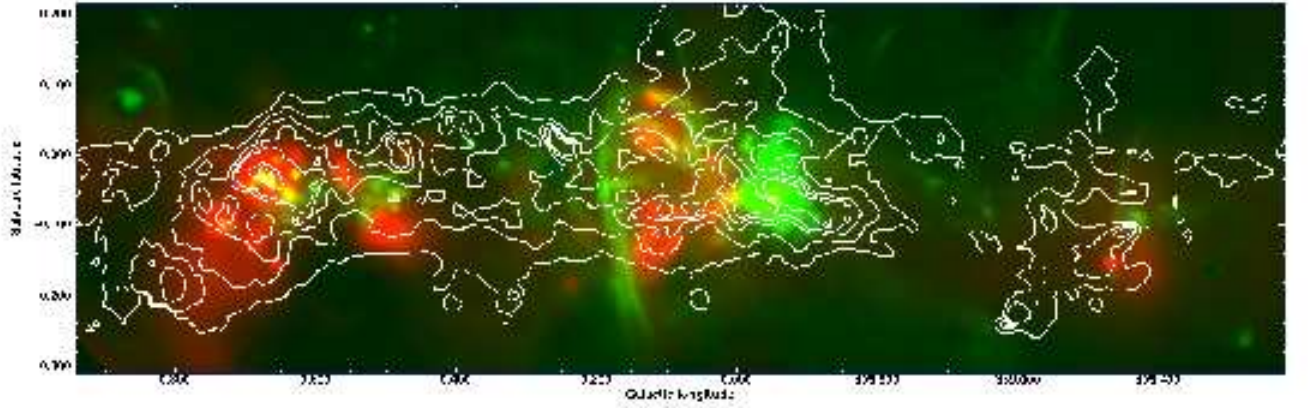
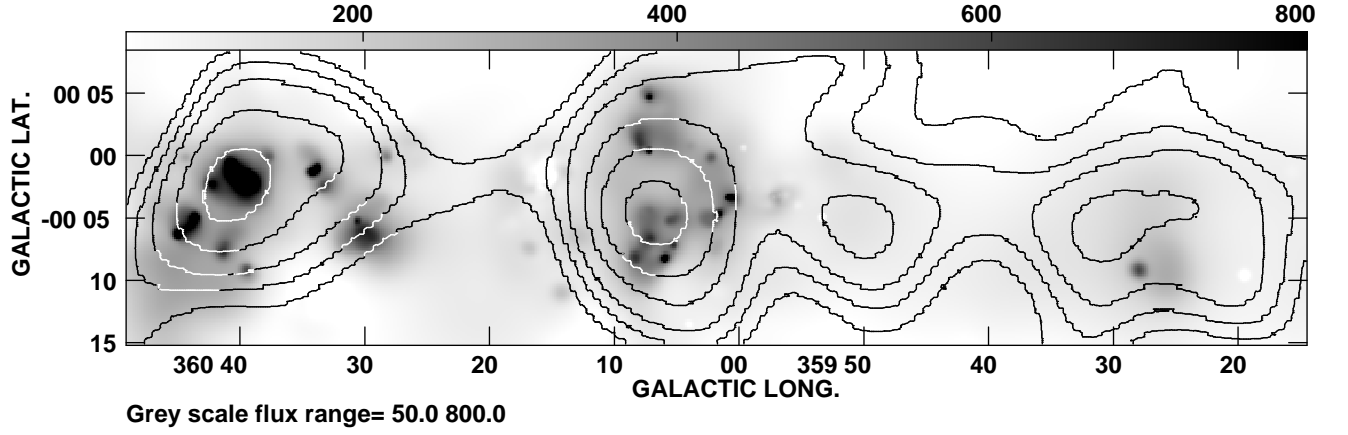


Fig. 12.— (a) Contours of HESS emission from the Galactic center (Aharonian et al. 2006) is superimposed on the distribution of $K\alpha$ 6.4 keV EW line emission. (b) Contours of 850 micron submillimeter emission are superimposed on the distributions of $K\alpha$ 6.4 keV EW line emission (in red) and a 20 cm continuum emission (in green color).

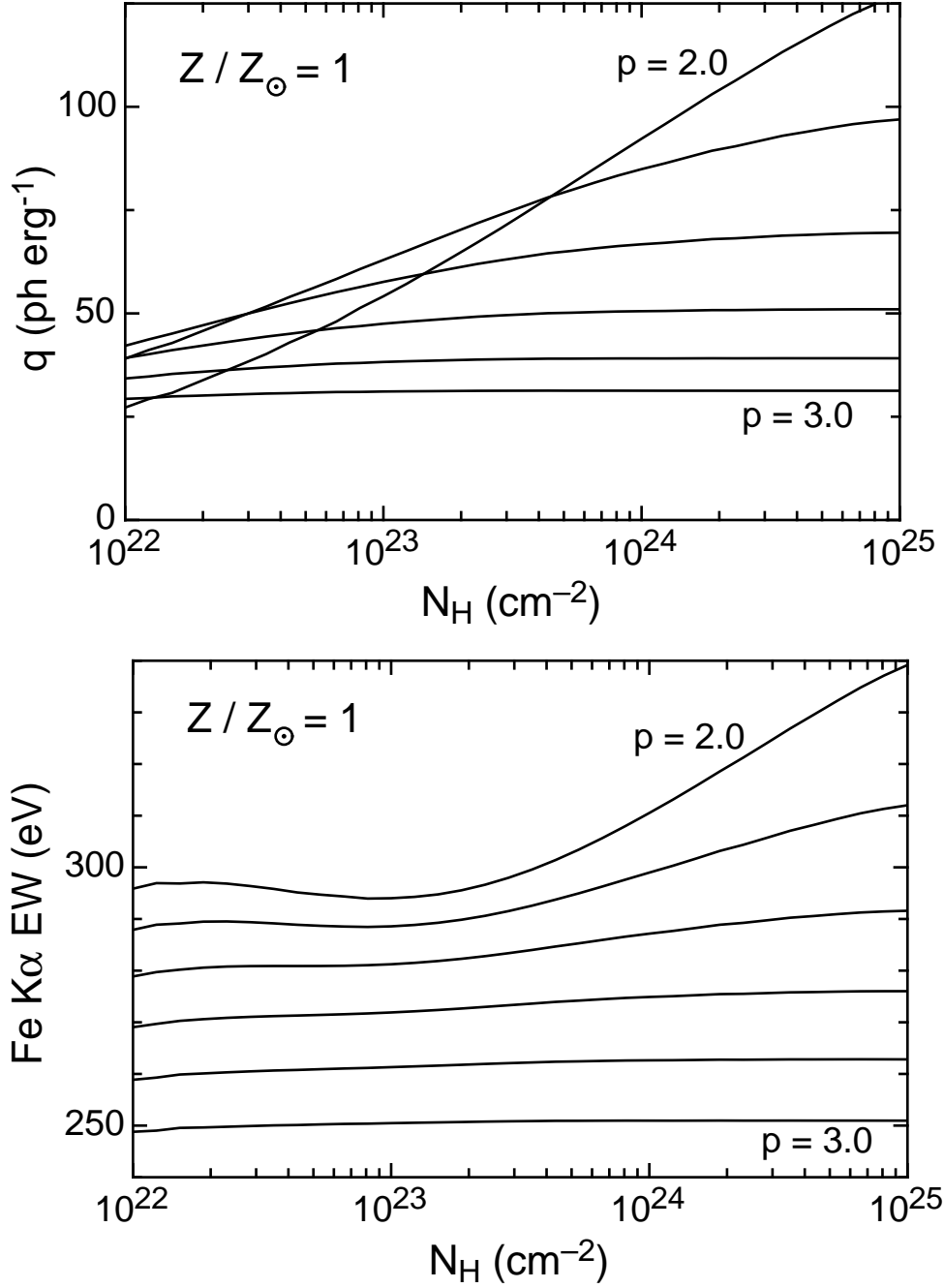


Fig. 13.— **a** Fe K α production per erg of electron energy injected into a cloud of given column density N_H and a solar iron abundance ($\text{Fe}/\text{H} = 2.8 \times 10^{-5}$). The curves are labeled by the power-law index p of the electron energy spectrum ($\propto E^{-p}$), which is assumed to run from 10 keV to 1 GeV. **b** Similar to (a) except that the equivalent width of Fe K α is shown as a function of column density for different values of the particle spectral index.

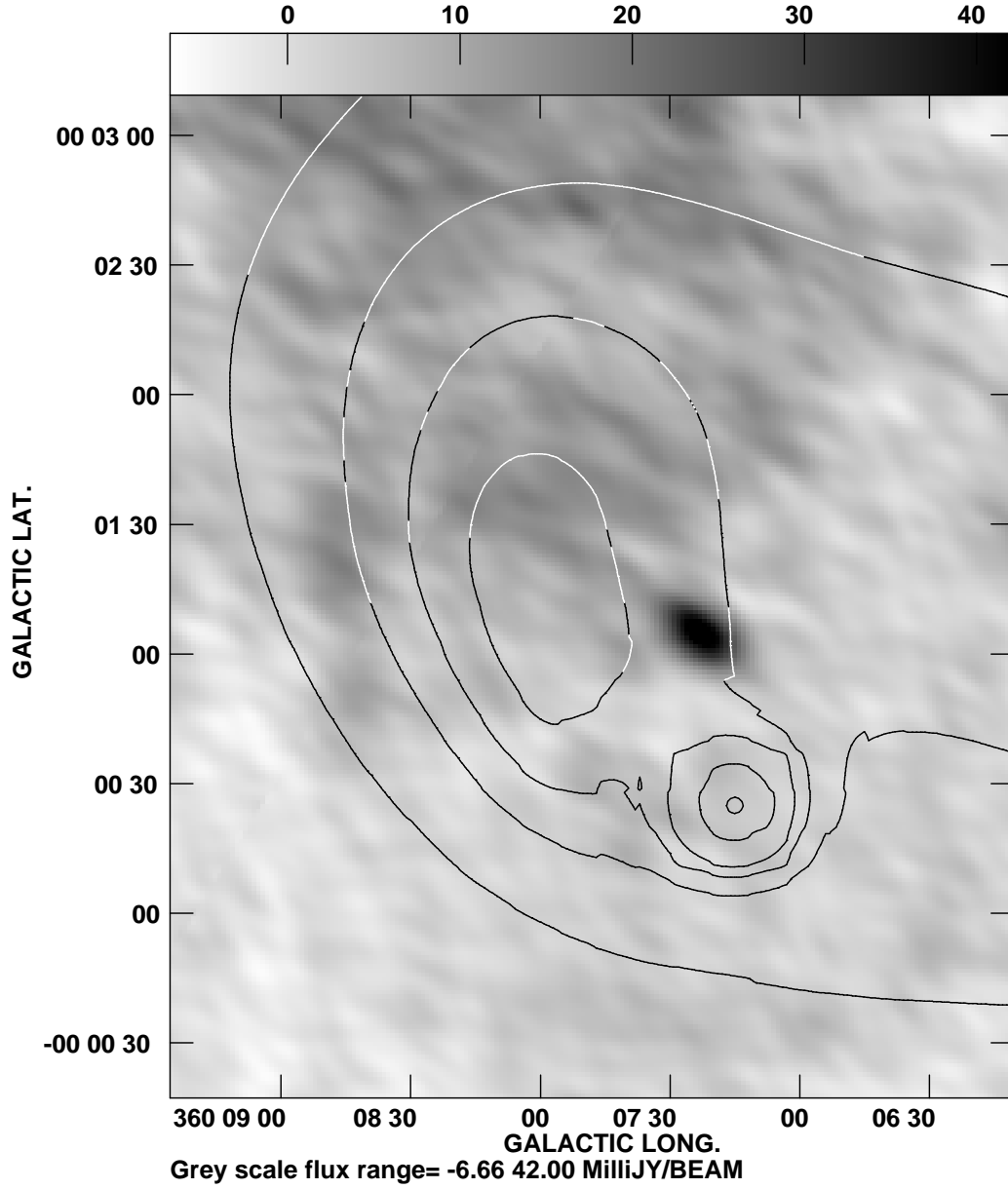


Fig. 14.— Contours of EW of Fe K α line emission with levels (3, 4, 5, 6, 8, 10) \times 100 eV are superimposed on a grayscale distribution of 90 cm emission from the Arches cluster (in black color).

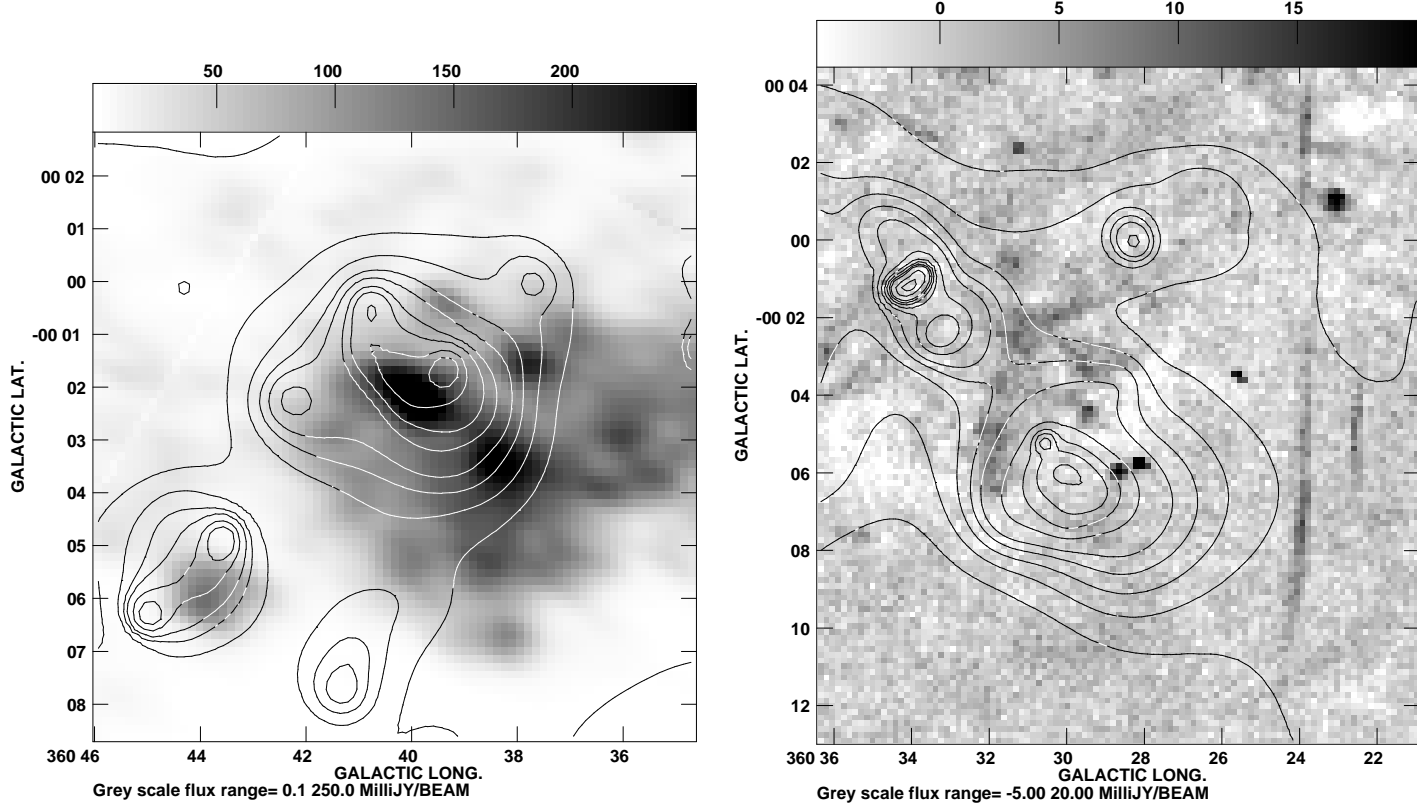


Fig. 15.— **a** Contours of EW of Fe K α line emission from Sgr B2 with levels (1, 2, 3, 4, 5, 6, 8, 10, 14, 18, 22) \times 100 eV are superimposed on a grayscale distribution of 90 cm emission from Sgr B2 with a resolution of $41.7'' \times 22.7''$ (PA= -6°) (Anantharamaiah et al. 1991). **b** Contours of EW of Fe K α line emission from Sgr B1 with levels (1, 1.5, 2, 2.5, 3, 4, 5, 6, 7, 8, 11, 14) \times 100 eV are superimposed on a grayscale distribution of 90 cm emission from Sgr B1 and G0.6-0.0 in black color with a resolution of $12.6 \times 6.8''$ (PA= 3°).